

CAIRNS: The Cluster And Infall Region Nearby Survey I. Redshifts and Mass Profiles

Kenneth Rines¹, Margaret J. Geller², Michael J. Kurtz², and Antonaldo Diaferio³

krines@cfa.harvard.edu

ABSTRACT

The CAIRNS (Cluster And Infall Region Nearby Survey) project is a spectroscopic survey of the infall regions surrounding eight nearby, rich, X-ray luminous clusters of galaxies. We collect 15665 redshifts (3471 new or remeasured) within $\sim 5 - 10 h^{-1} \text{Mpc}$ of the centers of the clusters, making it the largest study of the infall regions of clusters. We determine cluster membership and the mass profiles of the clusters based on the phase space distribution of the galaxies. All of the clusters display decreasing velocity dispersion profiles. The mass profiles are fit well by functional forms based on numerical simulations but exclude an isothermal sphere. Specifically, NFW and Hernquist models provide good descriptions of cluster mass profiles to their turnaround radii. Our sample shows that the predicted infall pattern is ubiquitous in rich, X-ray luminous clusters over a large mass range. The caustic mass estimates are in excellent agreement with independent X-ray estimates at small radii and with virial estimates at intermediate radii. The mean ratio of the caustic mass to the X-ray mass is 1.03 ± 0.11 and the mean ratio of the caustic mass to the virial mass (when corrected for the surface pressure term) is 0.93 ± 0.07 . We further demonstrate that the caustic technique provides reasonable mass estimates even in merging clusters.

Subject headings: galaxies: clusters: individual (A119, A147, A168, A194, A496, A539, A576, A1367, A1656 (Coma), A2197, A2199) — galaxies: kinematics and dynamics — cosmology: observations

¹Harvard-Smithsonian Center for Astrophysics, 60 Garden St, MS 10, Cambridge, MA 02138 ; krines@cfa.harvard.edu

²Smithsonian Astrophysical Observatory; mgeller, mkurtz@cfa.harvard.edu

³Università degli Studi di Torino, Dipartimento di Fisica Generale “Amedeo Avogadro”, Torino, Italy; diaferio@ph.unito.it

1. Introduction

Clusters of galaxies are the most massive gravitationally relaxed systems in the universe. They offer a unique probe of the properties of galaxies and the distribution of matter on intermediate scales. The dynamically relaxed centers of clusters are surrounded by infall regions in which galaxies are bound to the cluster but are not in equilibrium. These galaxies populate a regime between that of relaxed cluster cores and the surrounding large-scale structure where the transition from linear to non-linear clustering occurs. Recently, various investigators have explored infall regions using two-body dynamics of binary clusters (e.g. Mohr & Wegner 1997), the virial theorem in superclusters (Small et al. 1998), weak lensing (Kaiser et al. 2003), and caustics in redshift space (Geller et al. 1999; Reisenegger et al. 2000; Rines et al. 2000; Koranyi & Geller 2000; Drinkwater et al. 2001; Tustin et al. 2001; Rines et al. 2001a,b, 2002; Biviano & Girardi 2003).

In redshift space, the infall regions of clusters form a characteristic trumpet-shaped pattern. The presence of sharp features in redshift space near clusters in early redshift surveys hinted at the existence of such a pattern (Kent & Gunn 1982; de Lapparent et al. 1986; Ostriker et al. 1988). These features arise because galaxies fall into the cluster as the cluster potential overwhelms the Hubble flow (Kaiser 1987; Regös & Geller 1989). Under simple spherical infall, the galaxy phase space density becomes infinite at the location of these features, which were therefore termed caustics. Diaferio & Geller (1997, hereafter DG) and Diaferio (1999, hereafter D99) analyzed the dynamics of infall regions with numerical simulations and found that in the outskirts of clusters, random motions due to substructure and non-radial motions make a substantial contribution to the amplitude of the caustics which delineate the infall regions. DG showed that the amplitude of the caustics is a measure of the escape velocity from the cluster; identification of the caustics therefore allows a determination of the mass profile of the cluster on scales $\lesssim 10h^{-1}\text{Mpc}$.

DG and D99 show that nonparametric measurements of caustics yield cluster mass profiles accurate to $\sim 50\%$ on scales of up to $10 h^{-1} \text{ Mpc}$. This method assumes only that galaxies trace the velocity field. Indeed, simulations suggest that little or no velocity bias exists on linear and mildly non-linear scales (Kauffmann et al. 1999a,b). Vedel & Hartwick (1998) used simulations to explore an alternative parametric analysis of the infall region using a maximum likelihood method. Their technique requires assumptions about the functional forms of the density profile and the velocity dispersion profile.

We discuss the Cluster And Infall Region Nearby Survey (CAIRNS), a redshift survey of the infall regions of 8 nearby galaxy clusters. Previous papers from this survey examine A576 (Rines et al. 2000), A2199/A2197 (Rines et al. 2001b, 2002), and A1656 (Coma; Geller et al. 1999; Rines et al. 2001a). We include new or remeasured redshifts for 3471 galaxies in

the infall regions of six of the eight clusters in this survey.

The CAIRNS project tests whether the caustic pattern described in DG and D99 is common in nearby rich clusters and thus evaluates the feasibility of measuring cluster mass profiles at large radii from redshift surveys using the caustic technique. Other goals of CAIRNS include (1) measuring the mass-to-light ratio as a function of scale (Rines et al. 2000, 2001a), (2) detecting substructures in infall regions as a probe of structure formation (Rines et al. 2001b, 2002), and (3) studying the dependence of the spectroscopic properties of galaxies on environment over a large range of densities.

CAIRNS also provides an important zero-redshift benchmark for comparison with more distant systems (e.g., Ellingson et al. 2001). The CNOC1 project assembled an ensemble cluster from X-ray selected clusters at moderate redshifts. The CNOC1 ensemble cluster samples galaxies up to ~ 2 virial radii (see Carlberg et al. 1997a; Ellingson et al. 2001, and references therein). The caustic pattern is easily visible in the ensemble cluster, but Carlberg et al. (1997a) apply only Jeans analysis to the cluster to determine an average mass profile. Recently, Biviano & Girardi (2003) analyzed cluster redshifts from the 2dF 100,000 redshift data release. They stacked 43 poor clusters to produce an ensemble cluster containing 1345 galaxies within 2 virial radii and analyzed the properties of the ensemble cluster with both Jeans analysis and the caustic technique. Biviano & Girardi (2003) find good agreement between the two techniques; the caustic mass profile beyond the virial radius agrees well with an extrapolation of the Jeans mass profile. In contrast to these studies, the CAIRNS clusters are sufficiently well sampled to apply the caustic technique to the individual clusters.

We describe the cluster sample in § 2. We describe the spectroscopic observations and the redshift catalogs in § 3. In § 4, we review the caustic technique and use it to estimate the cluster mass profiles. We compare the caustic mass profiles to simple parametric models in § 5. We compute the velocity dispersion profiles in § 6. We compare the caustic mass profiles to X-ray and virial mass estimators in § 7. We discuss our results and conclude in §8. We assume $H_0 = 100h \text{ km s}^{-1}$, $\Omega_m = 0.3$, $\Omega_\Lambda = 0.7$ throughout.

2. The CAIRNS Cluster Sample

We selected the CAIRNS parent sample from all nearby ($cz_\odot < 15,000 \text{ km s}^{-1}$), Abell richness class $R \geq 1$ (Abell et al. 1989), X-ray luminous ($L_X > 2.5 \times 10^{43} h^{-2} \text{ erg s}^{-1}$) galaxy clusters with declination $\delta > -15^\circ$. Using X-ray data from the X-ray Brightest Abell Clusters (XBACs) catalog (Ebeling et al. 1996a,b), the parent cluster sample contains 14 systems. We selected a representative sample of 8 of these 14 clusters (Table 1). The redshifts and

X-ray properties listed in Table 1 are from (Ebeling et al. 1996a), the velocity dispersions are from §3.2, and the richness classes are from Abell et al. (1989). The 6 clusters meeting the selection criteria but not targeted in CAIRNS because of limited observing time are: A193, A426, A2063, A2107, A2147, and A2657. The 8 CAIRNS clusters span a variety of morphologies, from isolated clusters (A496, A2199) to major mergers (A168, A1367). We also do not include AWM7, which meets all the requirements for inclusion but is not in the Abell catalog. Koranyi & Geller (2000) describe a large spectroscopic survey of AWM7.

The redshift and declination limits are set by the small aperture and the location of the 1.5-m Tillinghast telescope used for the vast majority of our spectroscopic observations. The richness minimum guarantees that the systems contain sufficiently large numbers of galaxies to sample the velocity distribution. The X-ray luminosity minimum guarantees that the systems are real clusters and not superpositions of galaxy groups (cf. the discussion of A2197 in Rines et al. 2001b, 2002). Three additional clusters with smaller X-ray luminosities (A147, A194 and A2197) serendipitously lie in the survey regions of A168 and A2199. A147 and A2197 lie at nearly identical redshifts to A168 and A2199; their dynamics are probably dominated by the more massive cluster (Rines et al. 2002). A194, however, is cleanly separated from A168 and we therefore analyze it as a ninth system. The inclusion of A194 extends the parameter space covered by the CAIRNS sample. The X-ray temperature of A194 listed in (Ebeling et al. 1996a) is an extrapolation of the $L_X - T_X$ relation; in Table 1 we therefore list the direct temperature estimate of Fukazawa et al. (1998) from *ASCA* data. Fukazawa et al. (1998) lists X-ray temperatures for 6 of the 8 CAIRNS clusters which agree with those listed in Ebeling et al. (1996a).

3. Observations

3.1. Spectroscopy

We have collected 15665 redshifts within a radius of $\sim 10h^{-1}\text{Mpc}$ of the 8 clusters in the CAIRNS sample. Of this total, 3471 are new or remeasured and 1621 were published in Rines et al. (2000) and Rines et al. (2002). New and remeasured redshifts were obtained with the FAST spectrograph (Fabricant et al. 1998) on the 1.5-m Tillinghast telescope of the Fred Lawrence Whipple Observatory (FLWO). FAST is a high throughput, long slit spectrograph with a thinned, backside illuminated, antireflection coated CCD detector. The slit length is $180''$; our observations used a slit width of $3''$ and a $300 \text{ lines mm}^{-1}$ grating. This setup yields spectral resolution of 6-8 Å and covers the wavelength range 3600-7200 Å. We obtain redshifts by cross-correlation with spectral templates of emission-dominated and absorption-dominated galaxy spectra created from FAST observations (Kurtz & Mink

1998). The typical uncertainty in the redshifts is 30 km s^{-1} .

To construct the primary target catalogs for all clusters except A1367, we selected targets from digitized images of the POSS I 103aE (red) plates. These catalogs are roughly complete to $E = 15 - 16$, although the star-galaxy classification and photometric uncertainties limit the completeness of these catalogs. We selected A1367 targets from the Zwicky catalog and the Automated Plate Scanner⁴ catalog of the POSS I O (blue) plates. The A1367 catalog is complete to $m_{Zw}=15.7$ within a radius of 6° of the center of A1367. Rines et al. (2002) discuss incompleteness in the APS catalog.

Where possible, we use CCD photometry to define more complete and accurate catalogs. Our redshift survey of A576 (Rines et al. 2000) is complete to Kron-Cousins $R=16.5$ in a $3^\circ \times 3^\circ$ square, and our redshift survey of Coma (Rines et al. 2001a) is complete to $K_s=12.2$ within a radius of 8° based on 2MASS isophotal magnitudes ($K_s=20 \text{ mag arcsec}^{-2}$ isophote).

An important difference between the FAST spectra collected for CAIRNS and those collected for other, larger redshift surveys (Colless et al. 2001; Stoughton et al. 2002) is that CAIRNS suffers no incompleteness due to fiber placement constraints. Another difference is that the long-slit FAST spectra sample light from larger fractions of galaxy areas than fiber spectra. Thus, the effects of aperture bias (e.g., Kochanek et al. 2003) on spectral classification are greatly reduced. Carter et al. (2001) show that a spectroscopic survey of field galaxies obtained with identical instrumentation in a similar redshift range contains no significant aperture bias.

3.2. Redshift Catalogs

We compiled redshifts from the literature as collected by the NASA/IPAC Extragalactic Database (NED⁵). We then matched the catalogs with a $10''$ search radius. When an object has a redshift from both FAST and NED, we select the FAST redshift for the sake of homogeneity. We inspect all matches with redshift differences of $|\Delta v| \geq 100 \text{ km s}^{-1}$ to determine whether the redshifts are for the same object (close pairs of galaxies can be erroneously matched to each other). When the targets are identical, we adopt the FAST redshift unless the cross-correlation R value (Kurtz & Mink 1998) is ≤ 3.0 , in which case we adopt the NED redshift. The sources of the literature redshifts are too numerous to list here. A119, A168, and A194 all lie in or near the first SDSS survey strip; the SDSS Early

⁴<http://aps.umn.edu>

⁵The NASA/IPAC Extragalactic Database is available at <http://nedwww.ipac.caltech.edu/index.html>

Data Release contributes a plurality of the literature redshifts.

We apply the prescription of Danese et al. (1980) to determine the mean redshift cz_{\odot} and projected velocity dispersion σ_p of each cluster from all galaxies within $1.5 h^{-1}\text{Mpc}$ (1 Abell radius or R_A) of its X-ray center listed in Table 1. We calculate σ_p in two different ways. 3σ clipping, an iterative process where we first calculate the mean and variance of the distribution, then remove all galaxies offset by more than 3σ from the mean, and repeat as necessary. The second technique is use of the caustics to define membership (see § 4.2). We then calculate σ_p using only the cluster members projected within r_{200} , the radius which encloses a mass density 200 times the critical density. Note that our estimates of r_{200} do not depend on σ_p . We list both estimates of σ_p in Table 1; the values of σ_p calculated from the caustic members are all smaller than those calculated with 3σ clipping. This result suggests that the caustic membership criterion is more restrictive and less sensitive to interlopers than 3σ clipping (see § 4.2). For consistency, we adopt the projected velocity dispersions from the caustic technique in all further analyses.

Table 2 describes the catalog areas and lists the number of redshifts N_{cz} in each catalog, the number N_{CAIRNS} obtained with FAST, and the number N_{mem} of cluster members inside the caustics and projected within r_{200} . Note that A119, A168, and A194 overlap significantly; the number of unique redshifts in the combined catalog of A119 and A168 (Table 3) is 5055 (855 new or remeasured). For each galaxy, Table 3 indicates which cluster is less than 5° away or “Both” if both A119 and A168 are closer than 5° . Note that this designation is not a membership classification. Tables 4, 5, 6, 7, and 8 contain the redshift catalogs for A194, A496, A539, A1367, and Coma respectively. Note that the redshift catalog for A194 includes only literature redshifts (2431 redshifts from the literature are included in Table 4 but are not in Table 3) along with some FAST redshifts also listed in Table 3. The redshift catalog of Coma supersedes the online catalog referred to in Rines et al. (2001a). Redshift catalogs for A576 and A2199 are available in Rines et al. (2000) and Rines et al. (2002). Because the redshift catalogs include substantial contributions from the literature, the sampling and completeness are not uniform. Table 2 therefore cannot be used to compare cluster richesses. Geller et al. (1999) show that imposing a magnitude limit on the redshift catalog around Coma does not affect the location of the caustics or the resulting mass profile. Similarly, imposing a magnitude limit to these redshift catalogs does not significantly affect any of our results.

3.3. The $\sigma_p - T_X$ Relation of CAIRNS Clusters

Figure 1 shows the $\sigma_p - T_X$ relation for the CAIRNS clusters along with the best-fit $\sigma_p - T_X$ relation (using orthogonal distance regression) of a large sample of groups and clusters (Xue & Wu 2000). Although the scatter is large, the CAIRNS clusters follow the same relation.

4. Calculating the Mass Profiles

4.1. Method

We briefly review the method DG and D99 developed to estimate the mass profile of a galaxy cluster by identifying its caustics in redshift space. The method assumes that clusters form in a hierarchical process. Application of the method requires only galaxy redshifts and sky coordinates. Toy models of simple spherical infall onto clusters produce sharp enhancements in phase space density. These enhancements, known as caustics, appear as a trumpet shape in scatter plots of redshift versus projected clustercentric radius (Kaiser 1987). DG and D99 show that random motions smooth out the sharp pattern expected from simple spherical infall into a dense envelope in the redshift-radius diagram (see also Vedel & Hartwick 1998). The edges of this envelope can be interpreted as the escape velocity as a function of radius. Galaxies outside the caustics are also outside the turnaround radius. The caustic technique provides a well-defined boundary between the infall region and interlopers; one may think of the technique as a method for defining membership that gives the cluster mass profile as a byproduct.

The amplitude $\mathcal{A}(r)$ of the caustics is half of the distance between the upper and lower caustics in redshift space. Assuming spherical symmetry, $\mathcal{A}(r)$ is related to the cluster gravitational potential $\phi(r)$ by

$$\mathcal{A}^2(r) = -2\phi(r) \frac{1 - \beta(r)}{3 - 2\beta(r)} \quad (1)$$

where $\beta(r) = \sigma_t(r)/\sigma_r(r)$ is the velocity anisotropy parameter and σ_t and σ_r are the tangential and radial velocity dispersions respectively. DG show that the mass of a spherical shell of radii $[r_0, r]$ within the infall region is the integral of the square of the amplitude $\mathcal{A}(r)$

$$GM(< r) - GM(< r_0) = F_\beta \int_{r_0}^r \mathcal{A}^2(x) dx \quad (2)$$

where $F_\beta \approx 0.5$ is a filling factor with a numerical value estimated from simulations. Variations in F_β lead to some systematic uncertainty in the derived mass profile (see D99 for a

more detailed discussion).

Operationally, we identify the caustics as curves which delineate a significant decrease in the phase space density of galaxies in the projected radius-redshift diagram. For a spherically symmetric system, taking an azimuthal average amplifies the signal of the caustics in redshift space and smooths over small-scale substructures. We perform a hierarchical structure analysis to locate the centroid of the largest system in each cluster. We adaptively smooth the azimuthally averaged data and choose a threshold phase space density. The upper and lower caustics at a given radius are the redshifts at which this threshold density is exceeded when approaching the central redshift from the “top” and “bottom” respectively of the redshift-radius diagram. Because the caustics of a spherical system are symmetric, we adopt the smaller of the upper and lower caustics as the caustic amplitude $\mathcal{A}(r)$ at that radius. This procedure reduces the systematic uncertainties introduced by interlopers, which generally lead to an overestimate of the caustic amplitude. Rines et al. (2002) explore the effects of altering some of these assumptions and find that the differences are generally smaller than the estimated uncertainties.

D99 described this method in detail and showed that, when applied to simulated clusters containing galaxies modelled with semi-analytic techniques, it recovers the actual mass profiles to radii of 5-10 $h^{-1}\text{Mpc}$ from the cluster centers. D99 give a prescription for estimating the uncertainties in the caustic mass profiles. The uncertainties estimated using this prescription reproduce the actual differences between the caustic mass profiles and the true mass profiles. The uncertainties in the caustic mass profiles of observed clusters may be smaller than the factor of 2 uncertainties in the simulations. This difference is due in part to the large number of redshifts in the CAIRNS redshift catalogs relative to the simulated catalogs. Furthermore, the caustics are generally more cleanly defined in the data than in the simulations. Clearly, more simulations which better reproduce the appearance of observed caustics and/or include fainter galaxies would be useful in determining the limits of the systematic uncertainties in the caustic technique. In §7, we use the properties of the X-ray gas to determine the scatter in the caustic mass estimates relative to X-ray mass estimates.

4.2. Caustics in the CAIRNS Clusters

Figure 2 displays the projected radii and redshifts of galaxies surrounding the CAIRNS clusters, ordered left to right and top to bottom by decreasing X-ray temperature. The expected caustic pattern is easily visible in all systems; we calculate the shapes with the technique described in D99 using a smoothing parameter of $q = 25$. Previous investigations show that the mass profiles are insensitive to changes in the smoothing parameter (Geller

et al. 1999; Rines et al. 2000, 2002). Table 9 lists the hierarchical centers. These centers generally agree with the X-ray positions (Table 1) with a median difference of $56 h^{-1}\text{kpc}$ and with the redshift centers as determined using galaxies within R_A (Table 2) with a median difference of -0.0002. Figure 2 shows the caustics and Figure 3 shows the associated mass profiles. Note that the caustics extend to different radii for different clusters. D99 show that the appearance of the caustics depends strongly on the line of sight; projection effects can therefore account for most of the differences in profile shape seen in Figure 2 without invoking non-homology among clusters. We use the caustics to determine cluster membership. Here, the term “cluster member” refers to galaxies both in the virial region and in the infall region. Figure 2 shows that the caustics effectively separate cluster members from background and foreground galaxies, although some interlopers may lie within the caustics. This clean separation affirms our adoption of velocity dispersions calculated from cluster members as defined by the caustics (§3.2).

In the simulations of D99, the degree of definition of the caustics depends on the underlying cosmology; caustics are better defined in a low-density universe than a closed, matter-dominated universe. Surprisingly, the contrast of the phase space density between regions inside and outside the caustics is much stronger in the data than in both the τCDM and ΛCDM simulated clusters in D99. The difference may arise from the cosmological model used or the semi-analytic techniques for defining galaxy formation and evolution in the simulations. The difference may be accentuated by the large numbers of redshifts in the CAIRNS catalogs which extend (non-uniformly) to fainter magnitudes than the simulated catalogs displayed in D99. The definition of the caustics is unlikely to be a precise cosmological indicator, but it is suggestive that real clusters more closely resemble the ΛCDM than the τCDM simulated cluster.

The caustic pattern in the CAIRNS clusters is robust to the addition of fainter galaxies to the radius-redshift diagrams (see also Geller et al. 1999). This result suggests that dwarf galaxies trace the same caustic pattern as giant galaxies.

The D99 algorithm we use to identify the caustics does not always agree with the lines one might draw based on a visual impression. For instance, A496 contains many galaxies $6\text{-}9 h^{-1}\text{Mpc}$ from the center and at slightly lower redshift than the main body of the cluster. However, the D99 method finds no significant caustic amplitude beyond $4 h^{-1}\text{Mpc}$. One might expect the clump to indicate a large group or a poor cluster, but these galaxies show no strong concentration on the sky. We conclude that this apparent structure is not part of A496 but indicative of the surrounding large-scale structure. A2199 also contains many galaxies at the cluster redshift beyond the cutoff radius of the caustics as well as extensive substructure including X-ray groups. We discuss this system in detail in Rines et al. (2002).

The outskirts of A539 contain a number of galaxies at the cluster redshift but beyond the caustic cutoff radius. The caustic signal vanishes in the large radial gap at $3 h^{-1}\text{Mpc}$; the restriction on steepness of the caustics prevents the amplitude from rising again. Finally, the upper caustic of A168 encloses a relatively empty region of phase space. We discuss the individual clusters in more detail in §7.3.

4.3. Virial and Turnaround Radii

The caustic mass profiles allow direct estimates of the virial and turnaround radius in each cluster. For the virial radius, we calculate r_{200} , the density within which the enclosed average mass density is 200 times the critical density ρ_c . In our adopted cosmology, a system should be virialized inside the slightly larger radius $\sim r_{100} \approx 1.3r_{200}$ (Eke et al. 1996). We use r_{200} because it is more commonly used in the literature and thus allows easier comparison of results. For the turnaround radius r_t , we use equation (8) of Regös & Geller (1989) assuming $\Omega_m = 0.3$. For this value of Ω_m , the enclosed density is $3.5\rho_c$ at the turnaround radius. If the w parameter in the equation of state of the dark energy ($P_\Lambda = w\rho_\Lambda$) satisfies $w \geq -1$, the dark energy has little effect on the turnaround overdensity (Gramann & Suhonenko 2002). Varying Ω_m in the range 0.02–1 only changes the inferred value of r_t by $\pm 10\%$; the uncertainties in r_t from the uncertainties in the mass profile are comparable or larger (Rines et al. 2002).

Table 10 lists r_{200} , r_t , and the masses M_{200} and M_t enclosed within these radii. The mass of the infall region is 20–120% of the virial mass, demonstrating that clusters are still forming in the present epoch. Simulations of the future structure formation of the nearby universe (Gramann & Suhonenko 2002; Nagamine & Loeb 2003) for our assumed cosmology ($\Omega_m = 0.3, \Omega_\Lambda = 0.7$) suggest that galaxies currently inside the turnaround radius of a system will continue to be bound to that system. In open cosmologies with $\Omega_\Lambda = 0$, objects within which the enclosed density exceeds the critical density are bound, whereas in closed cosmologies, all objects are bound to all other objects.

One striking result of this analysis is that the caustic pattern is often visible beyond the turnaround radius of a cluster. This result suggests that clusters may have strong dynamic effects on surrounding large-scale structure beyond the turnaround radius. For our assumed cosmology, this large-scale structure is likely not bound to the cluster.

4.4. The Ensemble CAIRNS Cluster

Following other authors (e.g., Carlberg et al. 1997a; Biviano & Girardi 2003, and references therein), we construct an ensemble CAIRNS cluster to smooth over the asymmetries in the individual clusters. We construct two versions of the ensemble cluster, one including all 9 clusters and one excluding Coma, the best sampled cluster. This procedure ensures that our results are not biased by the inclusion of faint galaxies which are better sampled in Coma than in the other clusters. For both cases, we scale the velocities by σ_p (Table 2) and positions with the values of r_{200} determined from the caustic mass profiles (Table 10).

Figure 5 shows the caustic diagrams for the ensemble cluster including Coma. The ensemble cluster excluding Coma yields similar results, indicating that the results are robust to the addition of faint galaxies (see also Geller et al. 1999). The ensemble caustic mass profile yields similar results to the individual clusters. At r_{200} , the mass is $M_{200} = (2.4 \pm 0.6)\sigma_p^2 r_{200}/G$, consistent with the theoretical expectation of $M_{200} = 3\sigma_p^2 r_{200}/G$. The small difference suggests that either the measured velocity dispersions are larger than the true values (perhaps due to infalling, non-relaxed galaxies) or that the estimates of r_{200} are low.

The ensemble cluster contains 3907 members within the caustics; 1746 of these are projected within r_{200} and 1624 have projected radii between 1 and 5 r_{200} ($5r_{200}$ is comparable to the turnaround radii in Table 10). These results show that the number of galaxies in the infall region surrounding a cluster is comparable to the number projected within the virial region. Because the redshift surveys are more deeply sampled in the cluster centers, the infall region probably contains many more galaxies. The ensemble CAIRNS cluster contains more galaxies both within and outside r_{200} than either the CNOC1 ensemble cluster or that of Biviano & Girardi (2003).

5. Comparison to Simple Parametric Models

We fit the mass profiles of the CAIRNS clusters to three simple analytic models. The simplest model of a self-gravitating system is a singular isothermal sphere (SIS). The mass of the SIS increases linearly with radius. Navarro et al. (1997) and Hernquist (1990) propose two-parameter models based on CDM simulations of haloes. We note that the caustic mass profiles mostly sample large radii and are therefore not very sensitive to the inner slope of the mass profile. Thus, we do not consider alternative models which differ only in the inner slope of the density profile (e.g., Moore et al. 1999). At large radii, the NFW mass profile

increases as $\ln(r)$ and the mass of the Hernquist model converges. The NFW mass profile is

$$M(< r) = \frac{M(a)}{\ln(2) - \frac{1}{2}} \left[\ln\left(1 + \frac{r}{a}\right) - \frac{r}{a+r} \right] \quad (3)$$

where a is the scale radius and $M(a)$ is the mass within a . We fit the parameter $M(a)$ rather than the characteristic density δ_c ($M(a) = 4\pi\delta_c\rho_c a^3 [\ln(2) - \frac{1}{2}]$ where ρ_c is the critical density) because $M(a)$ and a are much less correlated than δ_c and a (Mahdavi et al. 1999). The Hernquist mass profile is

$$M(< r) = M \frac{r^2}{(r+a)^2} \quad (4)$$

where a is the scale radius and M is the total mass. Note that $M(a) = M/4$. The SIS mass profile is

$$M(< r) = M(a = 0.5 h^{-1}\text{Mpc}) \frac{r}{0.5 h^{-1}\text{Mpc}} \quad (5)$$

where we arbitrarily set the scale radius $a = 0.5 h^{-1}\text{Mpc}$. We minimize χ^2 and list the best-fit parameters a (fixed for SIS) and $M(a)$ for the three models in Table 11. We perform the fits on all data points within the turnaround radii listed in Table 10 and with caustic amplitude $\mathcal{A}^2(r) > 100 \text{ km s}^{-1}$. The caustic amplitude becomes negligible at a radius smaller than r_t in 4 of the 9 clusters.

Because the individual points in the mass profile are not independent, the absolute values of χ^2 (Table 11) are indicative only, but it is clear that the NFW and Hernquist profiles provide acceptable fits to the caustic mass profiles; the SIS is excluded for all clusters. The NFW profile provides a better fit to the data than the Hernquist profile for 4 of the 8 CAIRNS clusters plus A194; the other 4 are better fit by a Hernquist profile. A non-singular isothermal sphere mass profile yields results similar to the SIS; thus, we report only our results for the SIS. The concentration parameters $c = r_{200}/a$ for the NFW models are in the range 5–17, in good agreement with the predictions of numerical simulations (Navarro et al. 1997). There is no obvious correlation of c with mass, but the differences in c should be small ($\sim 20\%$ and with large scatter) over our mass range.

6. Velocity Dispersion Profiles

Several authors have explored the use of the velocity dispersion profile (VDP) of clusters as a diagnostic of their dynamical states. For example, Fadda et al. (1996) find that VDPs typically have three shapes: increasing, flat, or decreasing with radius.

We calculate the VDPs of the CAIRNS clusters using all galaxies inside the caustics. All the CAIRNS clusters display decreasing VDPs within about r_{200} (Figure 6). The VDPs either

flatten out or continue to decrease between r_{200} and r_t . Figure 6 also displays the predicted VDPs of the best-fit Hernquist mass models calculated assuming isotropic orbits. Because these predicted VDPs have no free parameters, they provide an interesting consistency check on our caustic mass profiles. The observed VDPs agree with the models for most clusters, even at radii much larger than r_{200} . The most significant difference is found in A2199, where the predicted VDP is smaller than the observed VDP. The observed VDP might be artificially enhanced by groups within the infall region (Rines et al. 2001b, 2002), or the caustic mass profile might be too small. Indeed, using the most massive profile from a more detailed study of this system (Rines et al. 2002) yields a predicted VDP that matches the observed VDP. Figure 7 shows that the predicted and observed VDPs of the ensemble cluster are in good agreement. This agreement suggests that the caustic mass profiles are consistent with Jeans analysis (see §7.2) and that the orbits are not far from isotropic, even outside the virial radius. However, this result could perhaps be mimicked by a population of infalling galaxies not in equilibrium and not on radial orbits. Indeed, many authors find evidence of an infalling population dominated by blue or emission line galaxies with larger velocity dispersions than the red and presumably more relaxed galaxies (Mohr et al. 1996; Carlberg et al. 1997b; Mahdavi et al. 1999; Koranyi & Geller 2000; Ellingson et al. 2001).

Some authors (Carlberg et al. 1997a; Girardi et al. 1998) claim that an accurate estimate of r_{200} can be obtained for a cluster from the asymptotic value of the velocity dispersion calculated for all galaxies within a given radius. Many of the CAIRNS clusters, however, display no obvious convergence in the enclosed velocity dispersion (shown by triangles in Figure 6). If the rich clusters in the CNOC1 survey are similar to their CAIRNS cousins, the use of the asymptotic value of the enclosed velocity dispersion to estimate r_{200} may be unreliable. The caustic technique provides an alternative method for estimating r_{200} , although applying it requires many more redshifts than are needed for computing the velocity dispersion.

7. Comparison to Other Mass Estimates

Because the caustic mass estimator is calibrated by simulations, it is important to test the accuracy of the estimator with independent observational mass estimates. Clusters usually possess a hot intracluster medium (ICM) with temperatures of 10^7 – 10^8 K. Assuming this hot gas is in hydrostatic equilibrium, one can estimate both the mass contained in hot gas and the total gravitational mass in the X-ray emitting region (Fabricant et al. 1980). The caustic method is completely independent of the X-ray properties of the clusters.

7.1. Mass and X-ray Temperature

The mass-temperature relation (Evrard et al. 1996; Horner et al. 1999; Nevalainen et al. 2000; Finoguenov et al. 2001) gives a straightforward estimate of the mass of a cluster from its X-ray temperature. We use the mass-temperature relation rather than, e.g., a β model to estimate the mass both for simplicity and to ensure uniformity (X-ray observations allowing more detailed mass estimates are not available for all CAIRNS clusters). Numerical simulations (Evrard et al. 1996) suggest that estimating cluster masses based solely on emission-weighted cluster temperatures yields similar accuracy and less scatter than estimates which incorporate density information from the surface brightness profile. In §7.3, we compare our results to more detailed X-ray mass estimates in the literature.

Finoguenov et al. (2001) find a relation of $M_{500} = (1.87 \pm 0.14) \times 10^{13} T_{keV}^{1.64 \pm 0.04} h^{-1} M_{\odot}$, where M_{500} is the enclosed mass within the radius r_{500} and T_{keV} is the emission-weighted electron temperature in keV. The X-ray temperature yields an estimate for r_{500} of $r_{500} = (0.32 \pm 0.01) \sqrt{T_{keV}} h^{-1} \text{Mpc}$. The temperatures of the four clusters in both their sample and ours are consistent. Figure 8 displays the interpolated caustic mass estimate at r_{500} (we derive r_{500} from T_{keV} rather than directly from the caustic mass profile) versus M_{500} from the mass-temperature relation. The agreement is generally good, with the exception of A576. The ratio of the caustic estimate to the X-ray estimate has an error-weighted mean of 1.03 ± 0.11 , indicating that the two methods are in excellent agreement. If we eliminate A576, an outlier in Figure 8, the error-weighted mean ratio is 0.97 ± 0.11 (Rines et al. 2000, discusses A576 in more detail). The scatter in the mass estimates of individual clusters is therefore $\sim 33\%$. The excellent agreement between the caustic technique and X-ray mass estimates confirms the prediction of D99 that the caustic mass estimate is unbiased. The relatively small scatter in the ratio suggests that the systematic uncertainty in the caustic technique is actually smaller than the factor of two suggested by simulations (see §4.1 and D99).

7.2. Virial and Projected Mass Estimates

Zwicky (1933, 1937) used the virial theorem to estimate the mass of the Coma cluster. With some modifications, notably a correction term for the surface pressure (The & White 1986), the virial theorem remains in wide use (e.g., Girardi et al. 1998, and references therein). Jeans analysis incorporates the radial dependence of the projected velocity dispersion (e.g., Carlberg et al. 1997a; van der Marel et al. 2000; Biviano & Girardi 2003, and references therein) and obviates the need for a surface term.

Jeans analysis and the caustic method are closely related. Both use the phase space distribution of galaxies to estimate the cluster mass profile. The primary difference is that the Jeans method assumes that the cluster is in dynamical equilibrium; the caustic method does not. The Jeans method depends on the width of the velocity distribution of cluster members at a given radius, whereas the caustic method calculates the edges of the velocity distribution at a given radius. The caustic method is not independent of the Jeans method, as the D99 method generally requires $\langle v_{esc}^2 \rangle_R \sim 4 \langle v^2 \rangle_R$ within the virial region with radius R (see D99 for a more detailed discussion). Mass estimates based on Jeans analysis thus provide a consistency check but not an independent verification of the caustic mass estimates.

Applying the Jeans method requires an assumption about either the mass distribution or the orbital distribution. Typically, one assumes that light traces mass and thus that the projected galaxy density is proportional to the projected mass density (e.g., Girardi et al. 1998) or one assumes a functional form for the orbital distribution (e.g., Biviano & Girardi 2003). Note that most authors make the implicit assumption that the orbital distribution of the dark matter can be inferred from that of the galaxies. Koranyi (2000) shows that galaxies in simulated clusters often have significantly different orbital distributions than the dark matter. Unfortunately, our redshift catalogs are highly non-uniform due to the use of data from the literature and due to the systematic uncertainties inherent in photographic photometry on large scales. This non-uniformity prevents an estimate of the projected galaxy density to a consistent magnitude limit.

We apply the virial mass and projected mass estimators (Heisler et al. 1985) to the CAIRNS clusters. For the latter, we assume the galaxies are on isotropic orbits. We must define a radius of virialization within which the galaxies are relaxed. We use r_{200} (Table 10) and include only galaxies within the caustics. We thus assume that the caustics provide a good division between cluster galaxies and interlopers (see Figure 2). We test the Jeans analysis on Coma by assuming a Hernquist profile and the scale radius from the caustic mass profile; we fit a constant anisotropy β and the core mass $M(a)$. The best-fit core mass is $39 \pm 5 \times 10^{13} h^{-1} M_\odot$ (68% confidence level), in excellent agreement with the core mass from the caustics. The best-fit anisotropy is $\beta = -0.4^{+0.6}_{-1.0}$, slightly tangentially anisotropic but consistent with isotropic orbits. For the ensemble cluster, the best-fit anisotropy is $\beta = -0.05^{+0.22}_{-0.27}$, again consistent with isotropic orbits. The best-fit core mass again agrees very well with the caustic mass profile. For this analysis, we calculate the VDPs from all galaxies within the caustics and within r_{200} . The caustics contain infalling galaxies which are not in equilibrium. Including these galaxies might result in an overestimate of the mass.

We calculate the virial mass according to

$$M_{vir} = \frac{3\pi}{2} \frac{\sigma_p^2 R_{PV}}{G} \quad (6)$$

where $R_{PV} = 2N(N-1)/\sum_{i,j>i} R_{ij}^{-1}$ is the projected virial radius and $\sigma_p^2 = \sum_i (v_i - \bar{v})^2/(N-1)$. If the system does not lie entirely within r_{200} , a surface pressure term 3PV should be added to the usual virial theorem so that $2T + U = 3PV$. The virial mass is then an overestimate of the mass within r_{200} by the fractional amount

$$C = 4\pi r_{200}^3 \frac{\rho(r_{200})}{\int_0^{r_{200}} 4\pi r^2 \rho dr} \left[\frac{\sigma_r(r_{200})}{\sigma(< r_{200})} \right]^2 \quad (7)$$

where $\sigma_r(r_{200})$ is the radial velocity dispersion at r_{200} and $\sigma(< r_{200})$ is the enclosed total velocity dispersion within r_{200} (e.g., Girardi et al. 1998). In the limiting cases of circular, isotropic, and radial orbits, the maximum value of the term involving the velocity dispersion is 0, 1/3, and 1 respectively.

The projected mass estimator is more robust in the presence of close pairs. The projected mass is

$$M_{proj} = \frac{32}{\pi G} \sum_i R_i (v_i - v)^2 / N \quad (8)$$

where we assume isotropic orbits and a continuous mass distribution. If the orbits are purely radial or purely circular, the factor 32 becomes 64 or 16 respectively. We estimate the uncertainties using the limiting fractional uncertainties $\pi^{-1}(2\ln N)^{1/2} N^{-1/2}$ for the virial theorem and $\approx 1.4N^{-1/2}$ for the projected mass. These uncertainties do not include systematic uncertainties due to membership determination or the assumption of isotropic orbits in the projected mass estimator. Table 12 lists the virial and projected mass estimates.

Figure 9 compares the projected mass estimates to the virial mass estimates. The two mass estimators generally give consistent results, but the uncertainties are probably underestimated. The error-weighted mean ratio of the estimates is $M_p/M_v = 1.18 \pm 0.05$. This result is not dominated by the outlier, A539. If we eliminate this data point, the mean ratio is 1.16 ± 0.05 . Similarly, Figures 10 and 11 compare these two estimators to the caustic mass estimates at r_{200} . The error-weighted mean ratios of these estimates are $M_c/M_v = 0.79 \pm 0.05$ and $M_c/M_p = 0.68 \pm 0.05$. The caustic mass estimates are consistent with virial mass estimates assuming a correction factor $C \approx 0.2M_{vir}$, consistent with the best-fit NFW profiles and in good agreement with Carlberg et al. (1997a), who estimate the correction needed for orbital distributions with constant β in the range $-0.50 \leq \beta \leq +0.75$. The squared velocity dispersion term in Equation 7 is ~ 0.10 - 0.33 for isotropic orbits (This term is a factor of 3 larger for purely radial orbits). The rest of the right-hand side of

Equation 7 varies from ~ 0.72 for $c=5$ to ~ 0.40 for $c=25$. Indeed, a crude estimate of C from these parameters (Table 12) yields excellent agreement with the caustic mass estimates, with an error-weighted mean of $M_c/M_{cv} = 0.93 \pm 0.07$ where $M_{cv} = (1 - C)M_v$ (Figure 12). The correction factor is $C=0.05\text{--}0.22$, but this correction factor could be larger by a factor of 3 for purely radial orbits. Such radially anisotropic orbits would, however, produce more steeply decreasing VDPs (see Girardi et al. 1998). This comparison confirms the indications from the VDPs (§6) that the caustic technique yields mass estimates consistent with Jeans analysis.

In their ensemble cluster, Biviano & Girardi (2003) found that the caustic mass at r_{200} is $\sim 60\%$ of the mass determined from Jeans analysis (restricted to galaxies with absorption-dominated spectra and assuming isotropic orbits) when they use a fixed value of $F_\beta(r) = 0.5$ to determine the caustic mass. If they use a non-constant $F_\beta(r)$ with a shape similar to that in Figure 3 of D99, the two mass estimates agree well. However, as shown above, the assumption of $F_\beta(r) = 0.5$ for the CAIRNS clusters yields caustic mass estimates consistent with Jeans analysis and in excellent agreement with the virial theorem if the surface pressure term is included. Also, using a non-constant $F_\beta(r)$ requires knowledge of r_{200} , whereas assuming a constant value does not. The caustics of the ensemble 2dF cluster appear to be flatter (less centrally peaked) than those of CAIRNS clusters; this difference, which perhaps reflects the difference in the typical cluster mass (CAIRNS clusters are generally more massive), may account for the different conclusions. Alternatively, aperture bias may cause Biviano & Girardi (2003) to include misclassified emission-dominated galaxies not in equilibrium in the Jeans analysis, thus biasing the Jeans mass toward larger values. However, we see no such bias in the above Jeans analysis of CAIRNS clusters despite making no attempt to remove infalling, non-equilibrium galaxies. Other possible differences include the deeper sampling of CAIRNS clusters and the relatively larger uncertainties in the scaling parameters in Biviano & Girardi (2003).

7.3. Individual Clusters

Previous studies have shown good agreement between caustic mass profiles and X-ray and virial estimates in individual systems: Coma (Geller et al. 1999), A576 (Rines et al. 2000), Fornax (Drinkwater et al. 2001), A1644 (Tustin et al. 2001), the Shapley Supercluster (RQCM), and A2199 (Rines et al. 2002). We discuss the five other CAIRNS clusters and A194 individually below.

7.3.1. Abell 119

In a previous study, Fabricant et al. (1993) demonstrate that A119 has a significant extension to the NE both in projected surface galaxy density and in X-ray emission. The redshift survey confirms that the overdensity of galaxies is at the same redshift as A119 and that it extends significantly farther to the NE than the study of Fabricant et al. (1993, see Rines et al. in preparation). Figure 13 shows the mass profile of A119. The caustic mass profile agrees very well with both X-ray and virial mass estimates compiled by Girardi et al. (1998). There are many other determinations of the mass of A119 from X-ray data, and they give a range of results. This range may result from calibration uncertainties in the various satellites: *Einstein* (White et al. 1997; Jones & Forman 1999), *ROSAT* and *ASCA* (Mohr et al. 1999; Finoguenov et al. 2001; Reiprich & Böhringer 2002), *ROSAT* and *Einstein* (Cirimele et al. 1997; Peres et al. 1998), and *BeppoSAX* (Ettori et al. 2002).

Because the virial masses calculated in §7.2 are based on the largest redshift samples currently available, we do not plot previous determinations of the virial masses in Figure 13 or similar figures in the following subsections.

7.3.2. Abell 168

Ulmer et al. (1992) studied the significance of X-ray-galaxy count offsets in clusters and concluded that A168 showed significant evidence of an offset, suggesting an ongoing merger between two roughly equal mass groups with different gas-to-galaxy ratios. We confirm this X-ray-optical offset in Table 9, where we find a separation of $239 h^{-1}\text{kpc}$ between the X-ray center and the hierarchical center of the galaxy distribution. Fadda et al. (1996) find that A168 contains three components in redshift space. Girardi et al. (1998) calculate the virial mass of A168 both in a joined and disjoined analysis (the joined analysis treats the system as a single body whereas the disjoined analysis treats the different redshift components as multiple systems). The joined peaks calculation yields $r_{vir} = 0.87 h^{-1}\text{Mpc}$ and $M_{vir} = 1.5 \pm 0.25 \times 10^{14} h^{-1} M_\odot$; the disjoined peaks have masses smaller by an order of magnitude. Figure 14 shows the mass estimates of the joined peaks analysis and the most massive of the three systems in the disjoined analysis. Our mass estimates exceed all of these estimates.

Figure 14 shows the mass estimated from the X-ray gas by White et al. (1997) and the estimate from the $M_{500} - T_X$ relation. Both estimates are smaller than the caustic mass at the same radii.

Our redshift survey shows that the offset between the peak of X-ray emission and galax-

ies at the cluster redshift is a real, physical offset (Rines et al. in preparation). Outside $1.7 h^{-1}\text{Mpc}$, the caustics of A168 are only constrained by the restriction on the derivative of $\mathcal{A}(r)$. This fact suggests that the caustic technique may be an unreliable measure of the membership in A168. We have previously shown that the caustic technique produces accurate estimates of mass profiles in minor mergers of well-separated clusters like the A2199/A2197 supercluster. The presence of an ongoing major merger in the center of A168 may heat the gas above a hydrostatic temperature; the X-ray temperature might thus be an inaccurate mass estimator. Alternatively, the caustic technique may fail in the presence of an ongoing major merger. Regardless of these issues, the difference is no larger than about a factor of two, well within the range of projection effects.

7.3.3. *Abell 496*

A496 has very symmetric X-ray emission. Markevitch et al. (1999) suggest that A496 and A2199 are prototypical relaxed clusters ideal for estimating mass profiles based on their symmetry, temperature profiles, and evidence for moderate cooling flows. Durret et al. (2000) analyze both X-ray data and a large catalog of redshifts and concur that A496 seems to be a relaxed cluster in both X-rays and in the galaxy distribution, with the possible exception of emission line galaxies. Like A119, there are many X-ray mass estimates of A496, all of which are shown in Figure 15. These estimates use data from various satellites: *Einstein* (Durret et al. 1994; White et al. 1997; Jones & Forman 1999), *ROSAT* (Durret et al. 2000), *ROSAT* and *ASCA* (Markevitch et al. 1999; Mohr et al. 1999; Finoguenov et al. 2001; Reiprich & Böhringer 2002), *ROSAT* and *Einstein* (Peres et al. 1998), and *BeppoSAX* (Ettori et al. 2002). The scatter in the X-ray estimates is significantly smaller than in A119, and the agreement with the caustic mass profile is excellent. We found similar agreement in A2199 (Rines et al. 2002), suggesting that X-ray emission from relaxed clusters yields very robust mass estimates.

7.3.4. *Abell 539*

In a study of A539, Ostriker et al. (1988) first looked for the caustic pattern around a cluster. Despite measuring several hundred redshifts, they were unable to place good constraints on the infall properties of A539. Even with the much larger redshift sample here, there are relatively few galaxies in the infall region of A539 (see Figure 2 and Table 10). The virial mass and projected mass estimator yield significantly different estimates of the mass of A539 (see Table 12), the largest difference of any of the CAIRNS clusters (Figure

9). The virial mass estimate of Girardi et al. (1998) is intermediate between our virial mass and projected mass estimates.

David et al. (1995, 1996) analyzed *ROSAT* X-ray observations of A539 and found an X-ray temperature of $1.3_{-0.3}^{+0.8}$ keV, unusually cool for a rich cluster. Assuming a hydrostatic-isothermal β model, David et al. (1995) found a cluster mass of $(1.0 \pm 0.5) \times 10^{14} h^{-1} M_\odot$, significantly smaller than virial mass estimates. David et al. (1996) are unable to resolve this discrepancy using simple models for the orbital distribution of the galaxies. X-ray observations of A539 using other instruments yield higher ICM temperatures, i.e., $3.0_{-0.4}^{+0.5}$ keV for *Einstein* MPC data (David et al. 1993) and 3.2 ± 0.1 keV (Vikhlinin et al. 1999) and 3.7 ± 0.3 keV (White 2000) for *ASCA* data. These comparisons suggest that the X-ray-optical mass discrepancy found in David et al. (1996) is due to a large systematic error in the *ROSAT* temperature determination. We therefore recalculate the estimate of David et al. (1996) using $T_X = 3.0$ keV and plot this estimate in Figure 16 along with X-ray mass estimates from *Einstein* data (White et al. 1997; Jones & Forman 1999), *ROSAT* and *ASCA* (Finoguenov et al. 2001; Reiprich & Böhringer 2002), and the $M_{500} - T_X$ relation. The X-ray mass estimates agree reasonably well with the caustic technique.

7.3.5. Abell 1367

Girardi et al. (1998) find that A1367 has multiple peaks in the velocity distribution. They calculate two masses for the main body of the system by assuming that the peaks are either joined or disjoined (i.e., one or two distinct bodies). Figure 17 shows the mass estimates of the joined peaks and the more massive of the disjoined peaks. The caustic mass profile is closer to the mass of the joined peaks but is consistent with the estimates of both the joined and disjoined peaks. The caustic technique is sensitive to the total interior mass and is thus more similar to the joined peaks analysis. The agreement of the two techniques suggests that the caustic technique is reasonably accurate even in the presence of significant velocity substructure in the center of a cluster.

Donnelly et al. (1998) use *ROSAT* and *ASCA* X-ray observations to show that A1367 is undergoing a merger of two subclusters. The X-ray image shows two peaks separated by $11'5 = 0.21 h^{-1} \text{Mpc}$ on the sky. The optical center we find from a hierarchical cluster analysis is located $4'$ N of the more X-ray luminous SE peak and $8'$ SE of the less luminous NW peak. The X-ray temperature varies significantly across the system and suggests that the ICM is shock heated, at least in the less luminous but hotter NW subcluster. The additional heating due to shocks and the presence of multiple peaks complicate the mass estimate. Donnelly et al. (1998) model the system as two distinct clusters and calculate

masses for each subcluster at radii of 0.25 and $0.50 h^{-1}\text{Mpc}$. Because the optical center is located between the X-ray peaks, we sum the masses of the subclusters to estimate the total mass of the system (the caustic technique should give the combined mass of all bodies in the system). Figure 17 shows the mass estimates derived using the observed X-ray temperature and gas distribution, but note that Donnelly et al. (1998) suggest that the mass might be lower by as much as $\sim 40\%$ if non-thermal heating is significant. White (2000) finds a flat temperature profile in A1367 consistent with an isothermal temperature of $4.0 \pm 0.5\text{keV}$, consistent with the temperature in Table 1.

Several authors have estimated the mass of A1367 without explicit discussion of substructure; we assume that these estimates are for the more luminous SE component. These estimates use data from various satellites: *Einstein* (White et al. 1997; Jones & Forman 1999), *ROSAT* and *ASCA* (Mohr et al. 1999), and *ROSAT* and *Einstein* (Peres et al. 1998). Figure 17 shows these estimates along with mass at r_{500} estimated using the $M_{500} - T_X$ relation.

The complexities described by Donnelly et al. (1998) suggest that X-ray mass estimates for A1367 could contain significant systematic uncertainties. Similarly, the velocity distribution is more complex than expected for a relaxed cluster (Girardi et al. 1998). The caustic technique yields a mass profile contained within the ranges of previous mass estimates based on optical and X-ray data. This result suggests that the caustic technique is effective even in complicated clusters containing significant substructure (see also Reisenegger et al. 2000; Rines et al. 2001b, 2002).

7.3.6. Abell 194

Abell 194 is a curious example of a cluster that is significantly elongated in both X-rays and in its galaxy distribution (see Chapman et al. 1988, and references therein). Chapman et al. (1988) show that A194 is anisotropic and investigate the effects of anisotropy on the virial mass estimator. They conclude that the virial mass of A194 is $1.8^{+0.8}_{-0.4} \times 10^{14} h^{-1} M_\odot$ where the asymmetric uncertainties reflect analytic calculations of the uncertainties due to an anisotropic galaxy distribution. Girardi et al. (1998) estimate a virial (corrected virial) mass of $7.0^{+2.5}_{-1.8}(6.0^{+2.2}_{-1.5}) \times 10^{13} h^{-1} M_\odot$ at $0.68 h^{-1}\text{Mpc}$. These estimates are consistent with our results. Finally, we note that Barton et al. (1998) detected two compact groups within A194, although they conclude that only one of them is a physical system, perhaps a cold core of galaxies in the center of the cluster potential.

White et al. (1997) find a mass of $2.5 \pm 1.1 \times 10^{13} h^{-1} M_{\odot}$ within $0.25 h^{-1} \text{Mpc}$ from a deprojection analysis of *Einstein* data. Nikogossyan et al. (1999) analyze multiwavelength observations of A194 and conclude that the significant elongation in the galaxy distribution is present only in the center of the cluster. They estimate a mass of $4.0_{-2.5}^{+6.0} \times 10^{13} h^{-1} M_{\odot}$ within $0.4 h^{-1} \text{Mpc}$ based on *ROSAT* PSPC data. Figure 18 displays the caustic mass profile of A194, the X-ray and optical estimates from §§7.1 and 7.2, and the X-ray estimates from the literature. The caustic mass profile agrees well with all other estimates, although the uncertainties are large.

8. Discussion

We catalog 15665 redshifts in the infall regions of eight rich, nearby, X-ray luminous clusters in CAIRNS along with A194, a “bonus” cluster in the foreground of one of the eight CAIRNS clusters. CAIRNS is the largest redshift survey of cluster infall regions to date. We find the following:

- The expected caustic pattern in redshift space is present in all systems.
- We use the shape of the caustics to calculate the mass profiles of the systems. These mass profiles yield estimates of the virial radii and the turnaround radii. The caustic pattern is often visible up to and beyond the turnaround radius. The mass in the infall region is 20–120% of the virial mass, showing that clusters are still forming.
- We stack the clusters to produce an ensemble cluster containing 1746 galaxies projected within r_{200} and an additional 1624 within $5r_{200}$ (roughly the turnaround radius). The infall region thus contains at least as many galaxies as the virial region.
- The caustic mass profiles agree with Hernquist and NFW models but exclude an isothermal sphere. Observed clusters resemble those in simulations, and their mass profiles are well described by extrapolations of NFW or Hernquist models out to the turnaround radius.
- The velocity dispersion profiles of the best-fit Hernquist mass profiles agree with the observed VDPs assuming isotropic orbits.
- The observed VDPs all decrease with radius within r_{200} .
- At small radii, the mass profiles agree with independent X-ray mass estimates with a mean ratio of 1.03 ± 0.11 .

- The scatter in the ratio of the caustic mass estimate to X-ray estimates in observations ($\sim 33\%$) appears to be smaller than the scatter in the ratio of the caustic mass estimate to the true mass profile in simulations ($\sim 50\%$).
- At larger radii, the caustic masses are smaller than projected masses and virial masses. However, the caustic masses agree with virial masses when the surface pressure term is taken into account (the mean ratio is 0.93 ± 0.07). The caustic masses agree with masses from Jeans analysis (assuming a Hernquist model) for both Coma and the ensemble cluster. These fits also indicate that the orbital distribution is close to isotropic.
- These results and those in the literature demonstrate the power of the caustic technique as a mass estimator over a large dynamic range in both mass and radius, from systems as small as the Fornax cluster ($5 - 9 \times 10^{13} M_{\odot}$; Drinkwater et al. 2001) to the most massive ($1 - 2 \times 10^{15} h^{-1} M_{\odot}$) clusters like Coma (Geller et al. 1999) and the Shapley Supercluster (Reisenegger et al. 2000).
- The mass profiles of individual clusters agree well with detailed X-ray mass estimates in the literature, and it is striking that A496, a relaxed cluster, shows the best agreement between caustic and X-ray mass estimates as well as the smallest scatter in the X-ray estimates. Two clusters, A168 and A1367, are probably undergoing major mergers. The caustic technique yields mass estimates comparable to other estimators even in these complex systems.

The CAIRNS project demonstrates that the caustic pattern is ubiquitous in rich, X-ray luminous galaxy clusters. The large 2dF and Sloan redshift surveys will provide large numbers of spectra which can be used to explore the caustic effect in a greater number and greater range of clusters. For instance, Biviano & Girardi (2003) analyze the 2dF 100,000 redshift data release and produce an ensemble cluster of 43 clusters generally less massive than the CAIRNS clusters. Because only $\sim 1\%$ of galaxies reside in rich clusters, the CAIRNS survey, which specifically targets clusters, actually yields more cluster redshifts than the 2dF 100,000 redshift data release. Future papers in the CAIRNS project will analyze the relative distributions of mass and light in cluster infall regions, X-ray and optical substructure within infall regions, and the dependence of spectroscopic properties on environment.

This project would not have been possible without the assistance of Perry Berlind and Michael Calkins, the remote observers at FLWO, and Susan Tokarz, who processed the spectroscopic data. We thank Dan Fabricant for orchestrating the design and construction of the FAST spectrograph which has kept the modest 1.5-m Tillinghast telescope surprisingly competitive. KR, MJG, and MJK are supported in part by the Smithsonian Institution. The

National Geographic Society - Palomar Observatory Sky Atlas (POSS-I) was made by the California Institute of Technology with grants from the National Geographic Society. This research has made use of the NASA/IPAC Extragalactic Database (NED) which is operated by the Jet Propulsion Laboratory, California Institute of Technology, under contract with the National Aeronautics and Space Administration. We thank Marion Schmitz at IPAC for pointing out errors in our online redshift catalog around Coma. We thank Dan Fabricant, Bill Forman, Lars Hernquist, Christine Jones, Andi Mahdavi, Joe Mohr, and Gary Wegner for helpful discussions. We thank Joe Mohr and Gary Wegner for the use of unpublished redshifts near A576 and A2199. We acknowledge the Max-Planck-Institut für Astrophysik in Garching for use of its computer facilities for some computations. We thank the referee for comments which improved the presentation of this paper.

REFERENCES

- Abell, G. O., Corwin, H. G., & Olowin, R. P. 1989, ApJS, 70, 1
- Barton, E. J., de Carvalho, R. R., & Geller, M. J. 1998, AJ, 116, 1573
- Biviano, A. & Girardi, M. 2003, ApJ, 585, 205
- Carlberg, R. G., Yee, H. K. C., & Ellingson, E. 1997a, ApJ, 478, 462
- Carlberg, R. G. et al. 1997b, ApJ, 476, L7
- Carter, B. J., Fabricant, D. G., Geller, M. J., Kurtz, M. J., & McLean, B. 2001, ApJ, 559, 606
- Chapman, G. N. F., Geller, M. J., & Huchra, J. P. 1988, AJ, 95, 999
- Cirimele, G., Nesci, R., & Trevese, D. 1997, ApJ, 475, 11
- Colless, M. et al. 2001, MNRAS, 328, 1039
- Danese, L., de Zotti, G., & di Tullio, G. 1980, A&A, 82, 322
- David, L. P., Jones, C., & Forman, W. 1995, ApJ, 445, 578
- . 1996, ApJ, 473, 692
- David, L. P., Slyz, A., Jones, C., Forman, W., Vrtilek, S. D., & Arnaud, K. A. 1993, ApJ, 412, 479

- de Lapparent, V., Geller, M. J., & Huchra, J. P. 1986, ApJ, 302, L1
- Diaferio, A. 1999, MNRAS, 309, 610
- Diaferio, A. & Geller, M. J. 1997, ApJ, 481, 633
- Donnelly, R. H., Markevitch, M., Forman, W., Jones, C., David, L. P., Churazov, E., & Gilfanov, M. 1998, ApJ, 500, 138
- Drinkwater, M. J., Gregg, M. D., & Colless, M. 2001, ApJ, 548, L139
- Durret, F., Adami, C., Gerbal, D., & Pislar, V. 2000, A&A, 356, 815
- Durret, F., Gerbal, D., Lachieze-Rey, M., Lima-Neto, G., & Sadat, R. 1994, A&A, 287, 733
- Ebeling, H., Voges, W., Boehringer, H., Edge, A. C., Huchra, J. P., & Briel, U. G. 1996a, MNRAS, 281, 799
- . 1996b, MNRAS, 283, 1103
- Eke, V. R., Cole, S., & Frenk, C. S. 1996, MNRAS, 282, 263
- Ellingson, E., Lin, H., Yee, H. K. C., & Carlberg, R. G. 2001, ApJ, 547, 609
- Ettori, S., De Grandi, S., & Molendi, S. 2002, A&A, 391, 841
- Evrard, A. E., Metzler, C. A., & Navarro, J. F. 1996, ApJ, 469, 494
- Fabricant, D., Cheimets, P., Caldwell, N., & Geary, J. 1998, PASP, 110, 79
- Fabricant, D., Kurtz, M., Geller, M., Zabludoff, A., Mack, P., & Wegner, G. 1993, AJ, 105, 788
- Fabricant, D., Lecar, M., & Gorenstein, P. 1980, ApJ, 241, 552
- Fadda, D., Girardi, M., Giuricin, G., Mardirossian, F., & Mezzetti, M. 1996, ApJ, 473, 670
- Finoguenov, A., Reiprich, T. H., & Böhringer, H. 2001, A&A, 368, 749
- Fukazawa, Y., Makishima, K., Tamura, T., Ezawa, H., Xu, H., Ikebe, Y., Kikuchi, K., & Ohashi, T. 1998, PASJ, 50, 187
- Geller, M. J., Diaferio, A., & Kurtz, M. J. 1999, ApJ, 517, L23
- Girardi, M., Giuricin, G., Mardirossian, F., Mezzetti, M., & Boschin, W. 1998, ApJ, 505, 74

- Gramann, M. & Suhonenko, I. 2002, MNRAS, 337, 1417
- Heisler, J., Tremaine, S., & Bahcall, J. N. 1985, ApJ, 298, 8
- Hernquist, L. 1990, ApJ, 356, 359
- Horner, D. J., Mushotzky, R. F., & Scharf, C. A. 1999, ApJ, 520, 78
- Jones, C. & Forman, W. 1999, ApJ, 511, 65
- Kaiser, N. 1987, MNRAS, 227, 1
- Kaiser, N., Wilson, G., Luppino, G., Kofman, L., Gioia, I., Metzger, M., & Dahle, H. 2003, ApJ, submitted (astro-ph/9809268)
- Kauffmann, G., Colberg, J. M., Diaferio, A., & White, S. D. M. 1999a, MNRAS, 303, 188
- . 1999b, MNRAS, 307, 529
- Kent, S. M. & Gunn, J. E. 1982, AJ, 87, 945
- Kochanek, C. S., Pahre, M. A., & Falco, E. 2003, ApJ, submitted (astro-ph/0011458)
- Koranyi, D. M. 2000, Ph.D. Thesis, Harvard University
- Koranyi, D. M. & Geller, M. J. 2000, AJ, 119, 44
- Kurtz, M. J. & Mink, D. J. 1998, PASP, 110, 934
- Mahdavi, A., Geller, M. J., Böhringer, H., Kurtz, M. J., & Ramella, M. 1999, ApJ, 518, 69
- Markevitch, M., Vikhlinin, A., Forman, W. R., & Sarazin, C. L. 1999, ApJ, 527, 545
- Mohr, J. J., Geller, M. J., Fabricant, D. G., Wegner, G., Thorstensen, J., & Richstone, D. O. 1996, ApJ, 470, 724
- Mohr, J. J., Mathiesen, B., & Evrard, A. E. 1999, ApJ, 517, 627
- Mohr, J. J. & Wegner, G. 1997, AJ, 114, 25
- Moore, B., Quinn, T., Governato, F., Stadel, J., & Lake, G. 1999, MNRAS, 310, 1147
- Nagamine, K. & Loeb, A. 2003, New Astronomy, 8, 439
- Navarro, J. F., Frenk, C. S., & White, S. D. M. 1997, ApJ, 490, 493
- Nevalainen, J., Markevitch, M., & Forman, W. 2000, ApJ, 532, 694

- Nikogossyan, E., Durret, F., Gerbal, D., & Magnard, F. 1999, A&A, 349, 97
- Ostriker, E. C., Huchra, J. P., Geller, M. J., & Kurtz, M. J. 1988, AJ, 96, 1775
- Peres, C. B., Fabian, A. C., Edge, A. C., Allen, S. W., Johnstone, R. M., & White, D. A. 1998, MNRAS, 298, 416
- Regös, E. & Geller, M. J. 1989, AJ, 98, 755
- Reiprich, T. H. & Böhringer, H. 2002, ApJ, 567, 716
- Reisenegger, A., Quintana, H., Carrasco, E. R., & Maze, J. 2000, AJ, 120, 523
- Rines, K., Geller, M. J., Diaferio, A., Mahdavi, A., Mohr, J. J., & Wegner, G. 2002, AJ, 124, 1266
- Rines, K., Geller, M. J., Diaferio, A., Mohr, J. J., & Wegner, G. A. 2000, AJ, 120, 2338
- Rines, K., Geller, M. J., Kurtz, M. J., Diaferio, A., Jarrett, T. H., & Huchra, J. P. 2001a, ApJ, 561, L41
- Rines, K., Mahdavi, A., Geller, M. J., Diaferio, A., Mohr, J. J., & Wegner, G. 2001b, ApJ, 555, 558
- Small, T. A., Ma, C., Sargent, W. L. W., & Hamilton, D. 1998, ApJ, 492, 45
- Stoughton, C. et al. 2002, AJ, 123, 485
- The, L. S. & White, S. D. M. 1986, AJ, 92, 1248
- Tustin, A. W., Geller, M. J., Kenyon, S. J., & Diaferio, A. 2001, AJ, 122, 1289
- Ulmer, M. P., Wirth, G. D., & Kowalski, M. P. 1992, ApJ, 397, 430
- van der Marel, R. P., Magorrian, J., Carlberg, R. G., Yee, H. K. C., & Ellingson, E. 2000, AJ, 119, 2038
- Vedel, H. & Hartwick, F. D. A. 1998, ApJ, 501, 509
- Vikhlinin, A., Forman, W., & Jones, C. 1999, ApJ, 525, 47
- White, D. A. 2000, MNRAS, 312, 663
- White, D. A., Jones, C., & Forman, W. 1997, MNRAS, 292, 419
- Xue, Y. & Wu, X. 2000, ApJ, 538, 65

Zwicky, F. 1933, *Helv. Phys. Acta*, 6, 110

—. 1937, *ApJ*, 86, 217

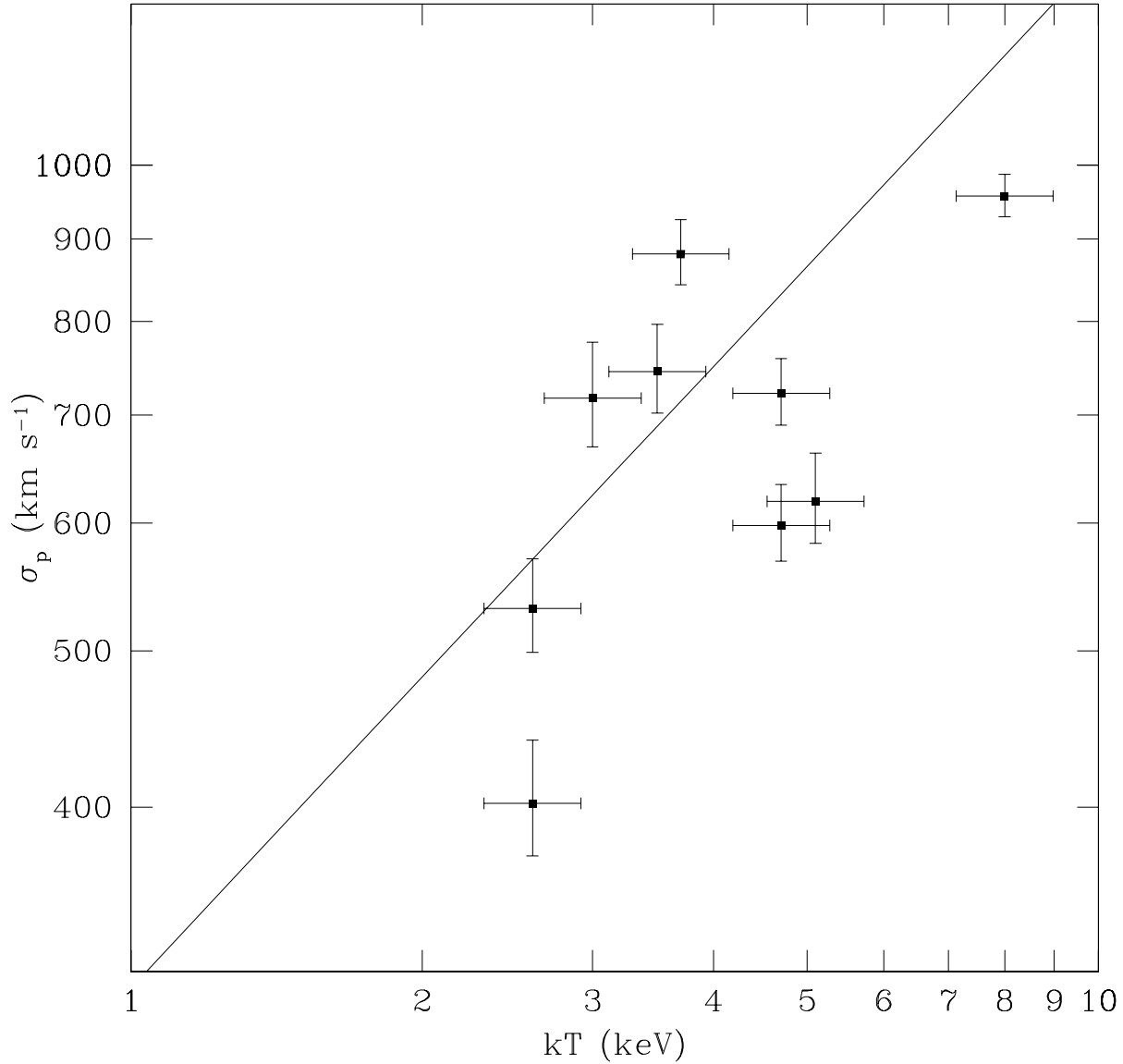


Fig. 1.— Velocity dispersion versus X-ray temperature for the CAIRNS clusters. The solid line shows the $\sigma - T_X$ relation of Xue & Wu 2000.

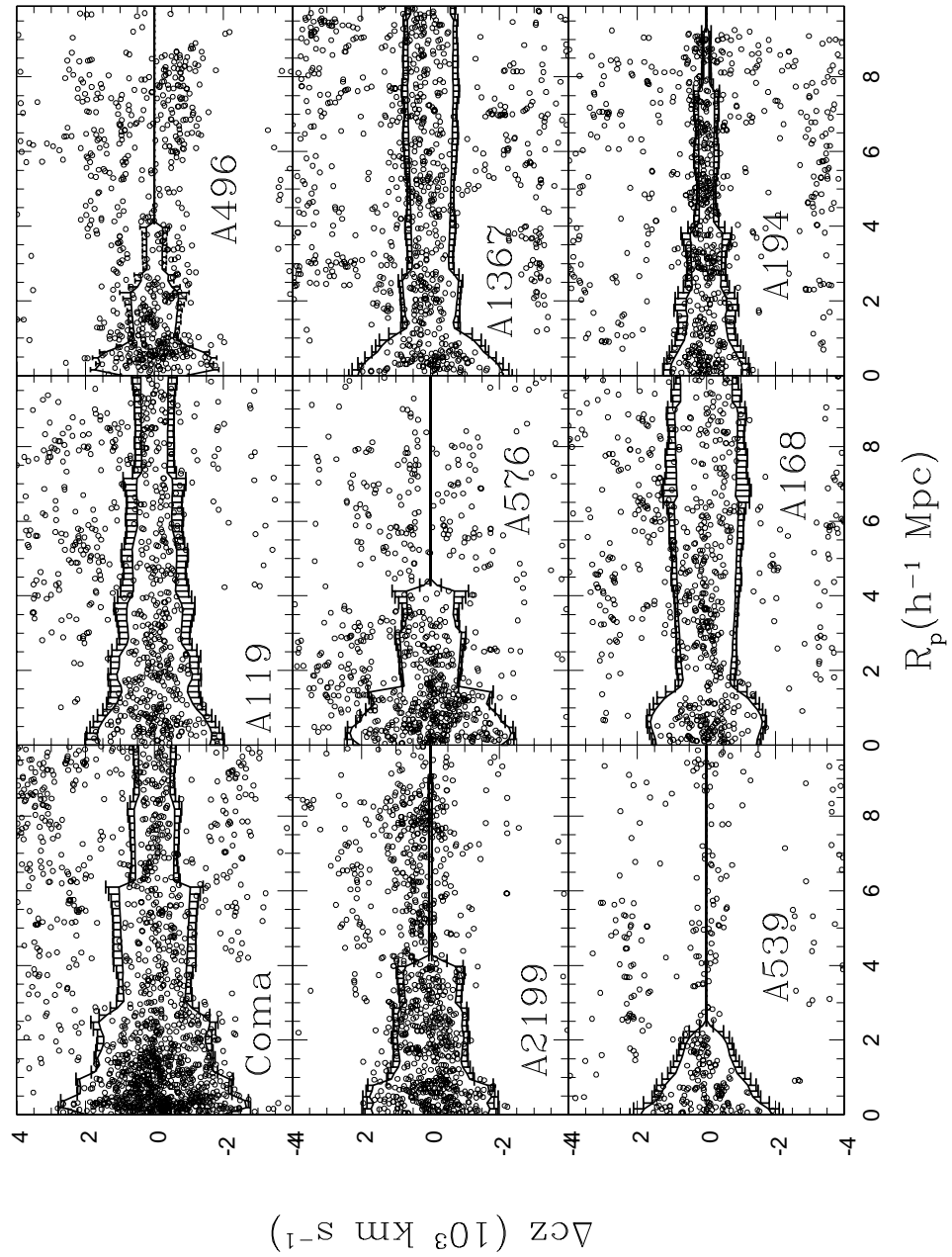


Fig. 2.— Redshift versus radius for galaxies around the CAIRNS clusters. The caustic pattern is evident as the trumpet-shaped regions with high density. The solid lines indicate our estimate of the location of the caustics in each cluster. The errorbars are $1-\sigma$ uncertainties and are shown only on one side of each caustic for clarity.

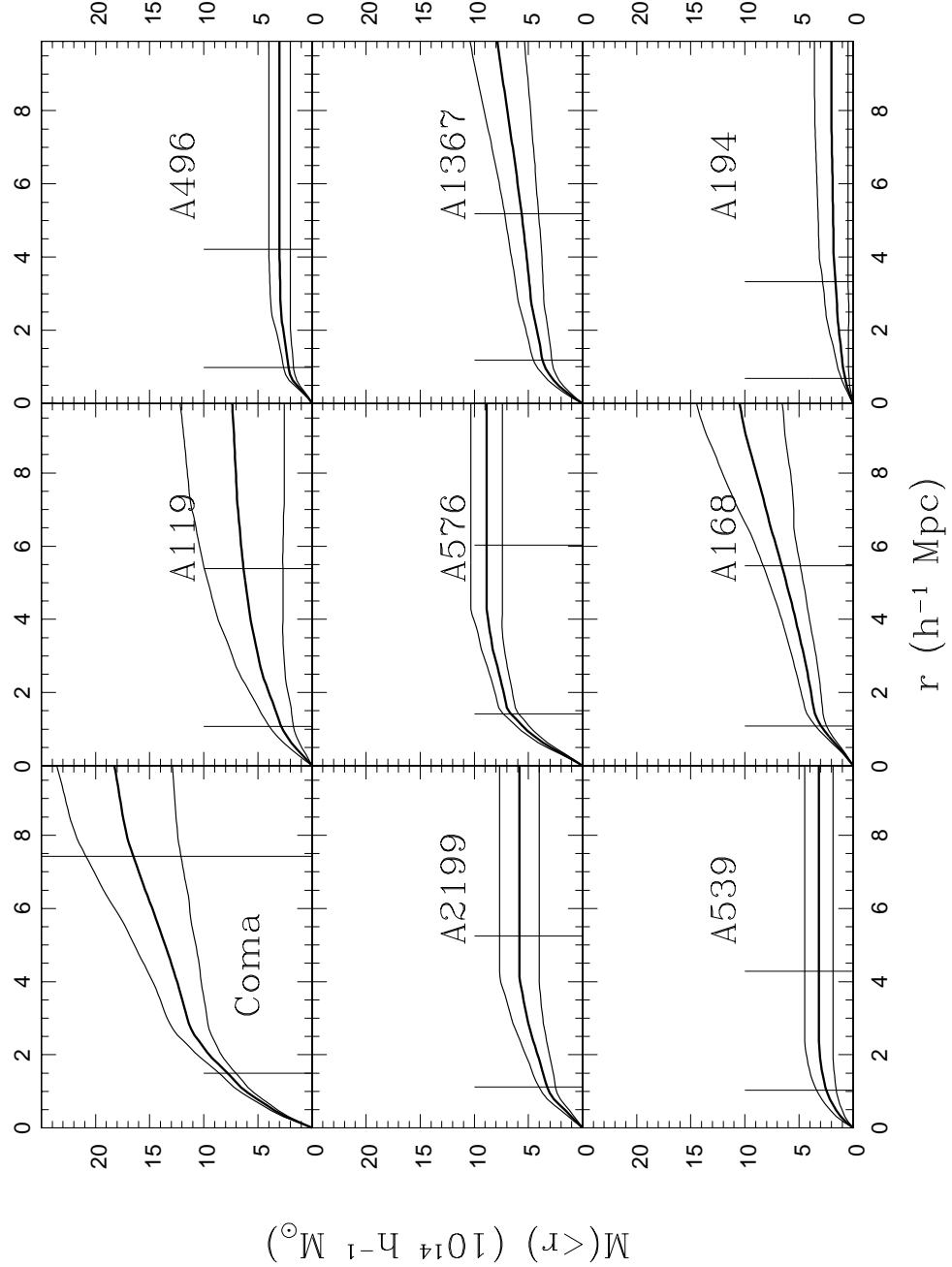


Fig. 3.— Caustic mass profiles for the CAIRNS clusters. The thick solid lines show the caustic mass profiles and the thin lines show the 1- σ uncertainties in the mass profiles. The axes are identical in all panels. The vertical bars indicate r_{200} and the turnaround radius.

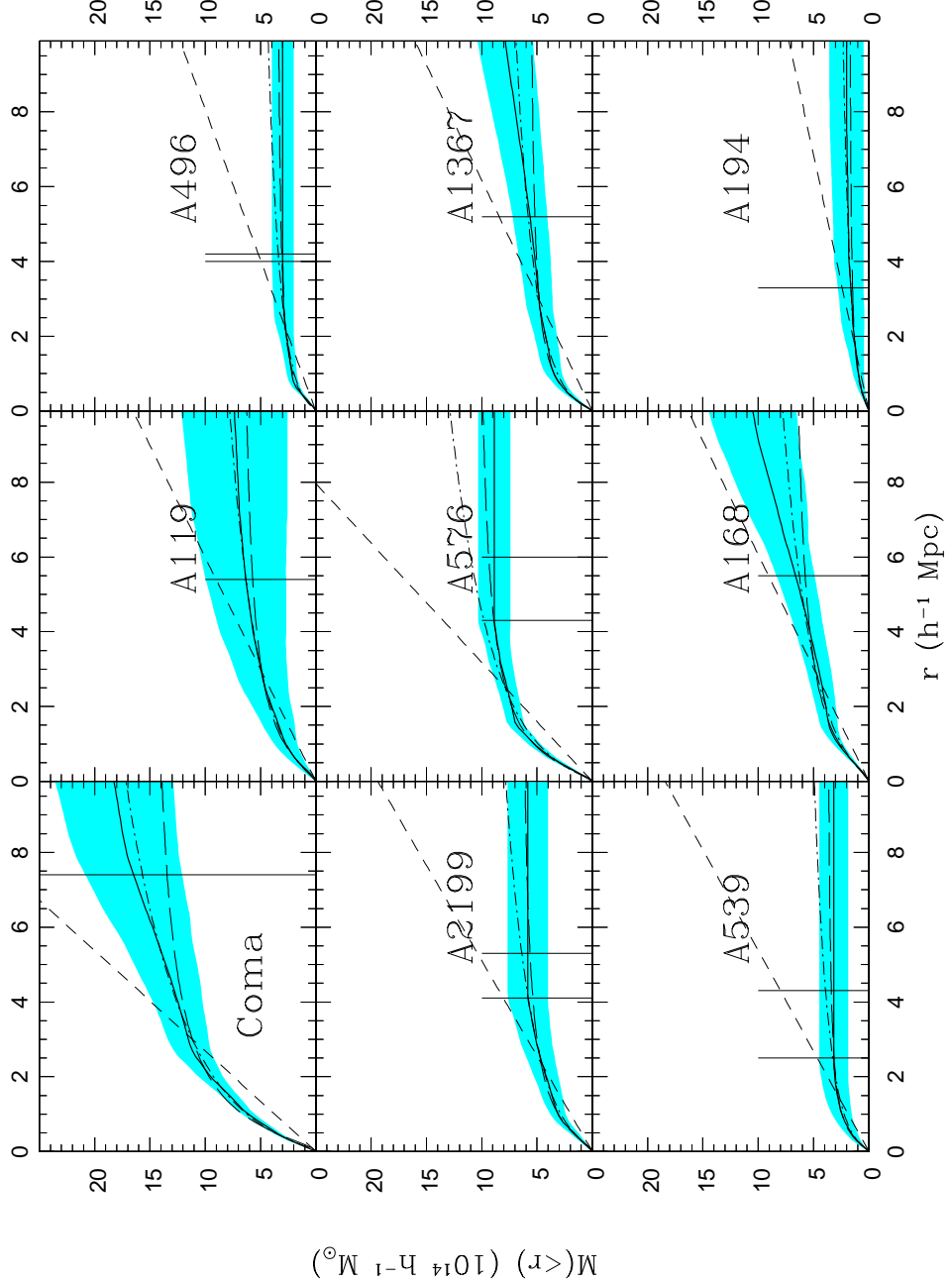


Fig. 4.— Caustic mass profiles for the CAIRNS clusters compared to simple models. The thick solid lines show the caustic mass profiles and the shaded region shows the $1-\sigma$ uncertainties in the mass profiles. The vertical bars indicate the turnaround radius and the limit of the caustics if it is smaller than the turnaround radius. The best-fit SIS, NFW, and Hernquist profiles are displayed as short-dashed, dash-dotted, and long-dashed lines respectively. The axes are identical in all panels.

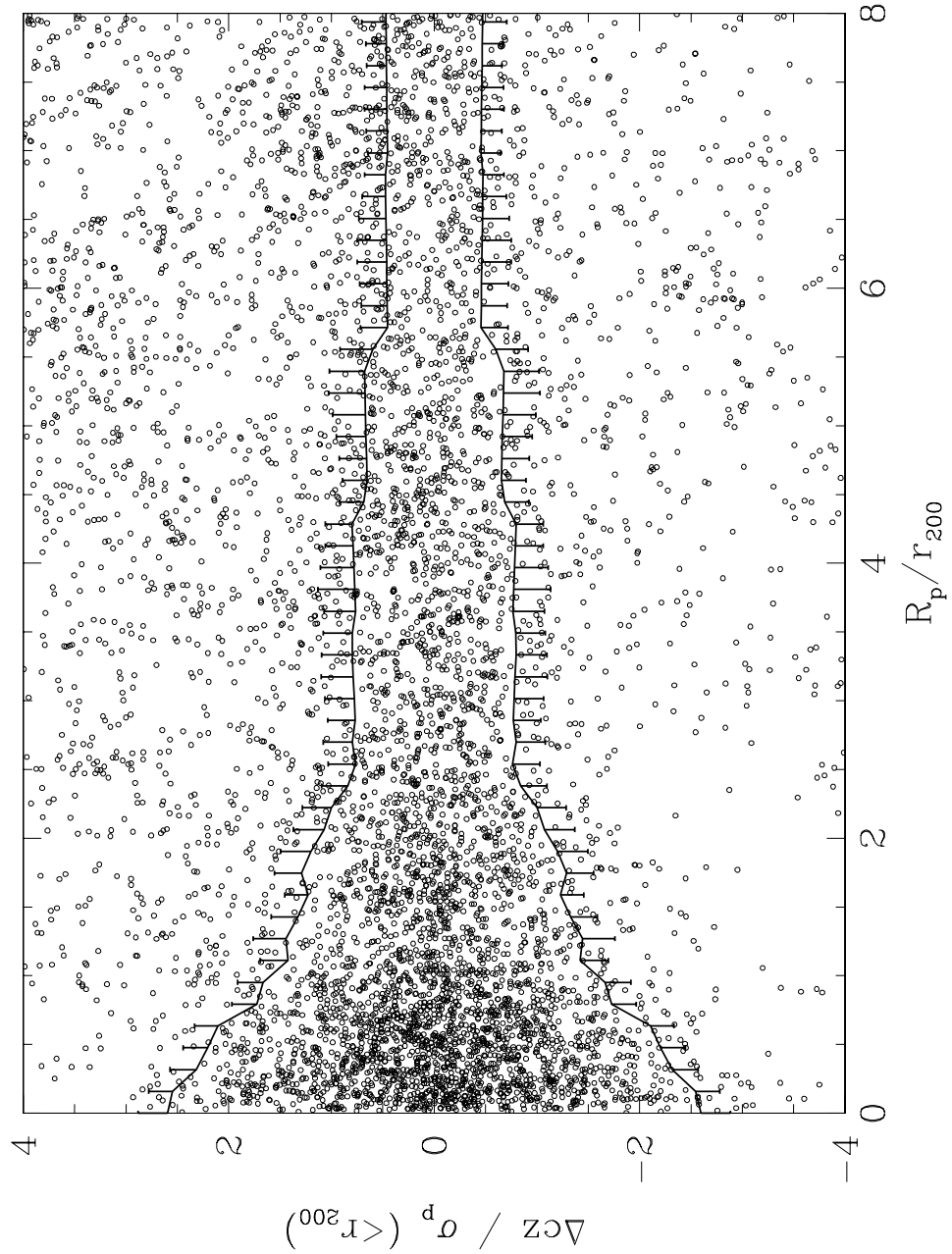


Fig. 5.— Redshift versus radius for galaxies around the CAIRNS ensemble cluster. The solid lines indicate our estimate of the location of the caustics. The errorbars are $1-\sigma$ uncertainties and are shown only on one side of each caustic for clarity.

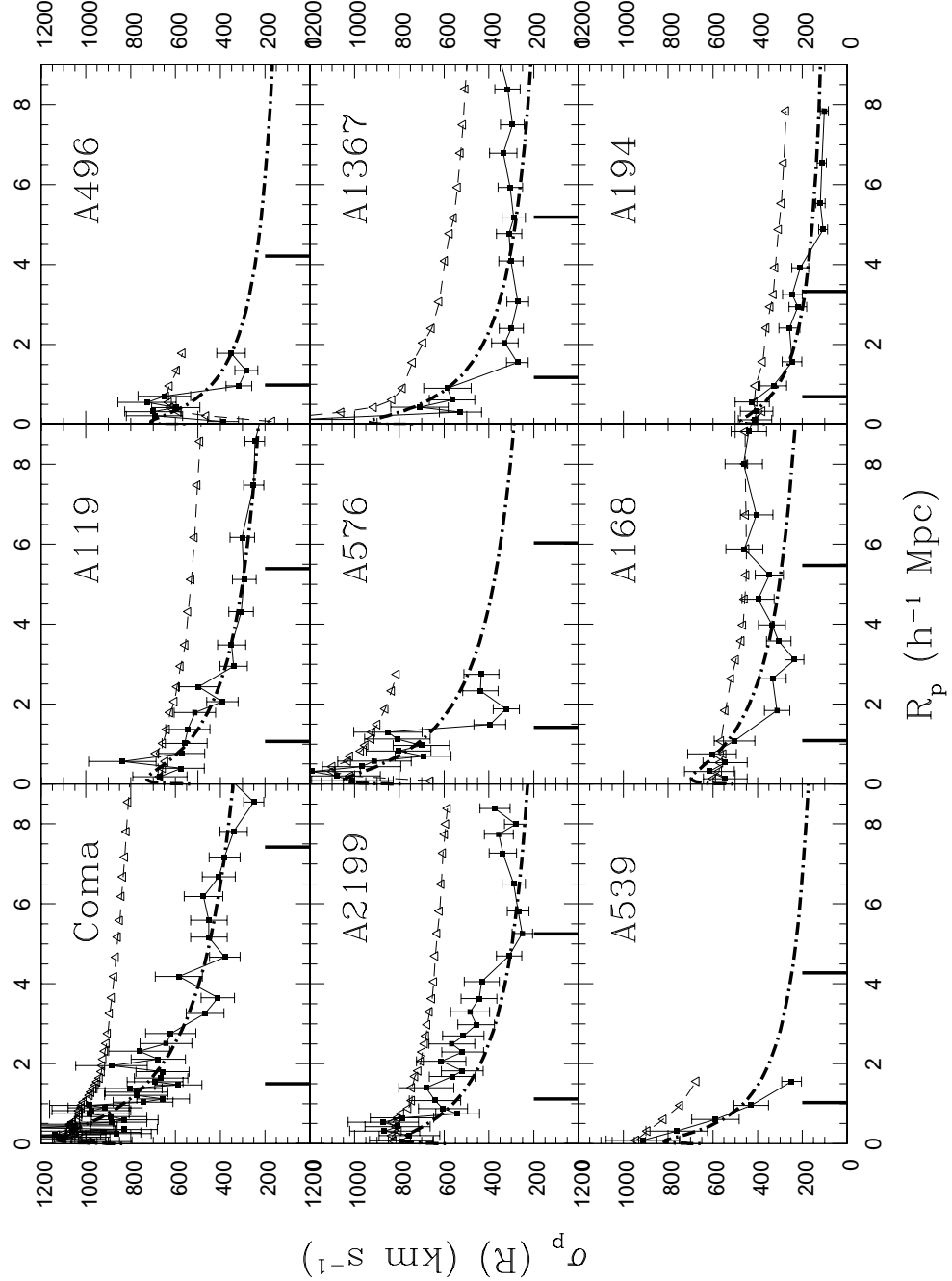


Fig. 6.— Velocity dispersion profiles for the CAIRNS clusters. The filled squares and solid lines show the velocity dispersion profile of member galaxies (those within the caustics) with $1-\sigma$ uncertainties. The open triangles and dashed lines show the enclosed velocity dispersion. The dash-dotted lines show the VDPs predicted by the Hernquist mass models which best fit the caustic mass profiles (assuming isotropic orbits). Heavy ticks on the abscissa indicate r_{200} and r_t . The axes are identical in all panels.

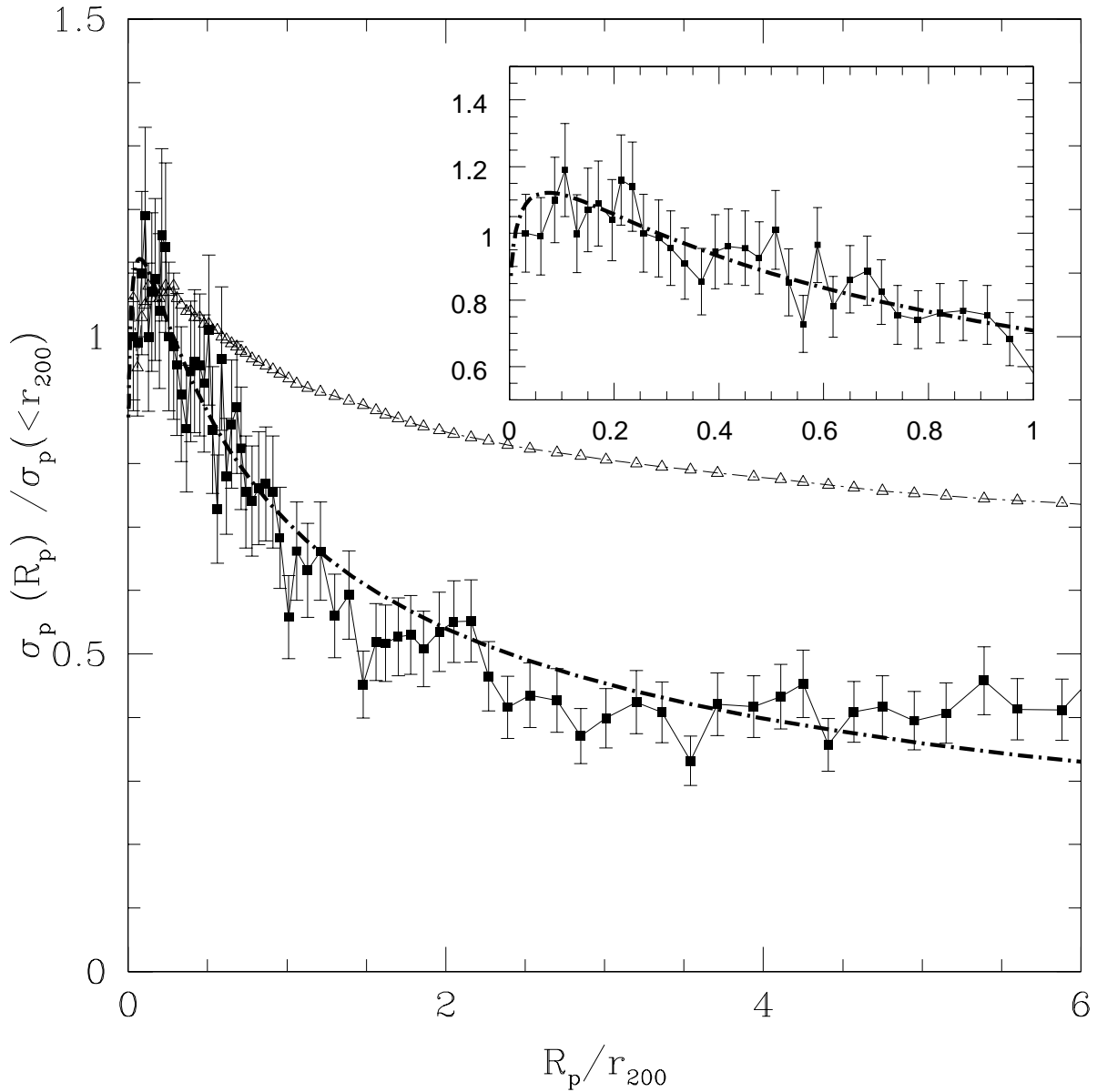


Fig. 7.— Velocity dispersion profile of the ensemble CAIRNS cluster. The filled squares and solid line show the velocity dispersion profile of member galaxies (those within the caustics) with $1-\sigma$ uncertainties. The open triangles and dashed line show the enclosed velocity dispersion. The dash-dotted line shows the VDP predicted by the Hernquist mass models which best fits the caustic mass profiles (assuming isotropic orbits). The inset shows a closeup of the VDP within r_{200} .

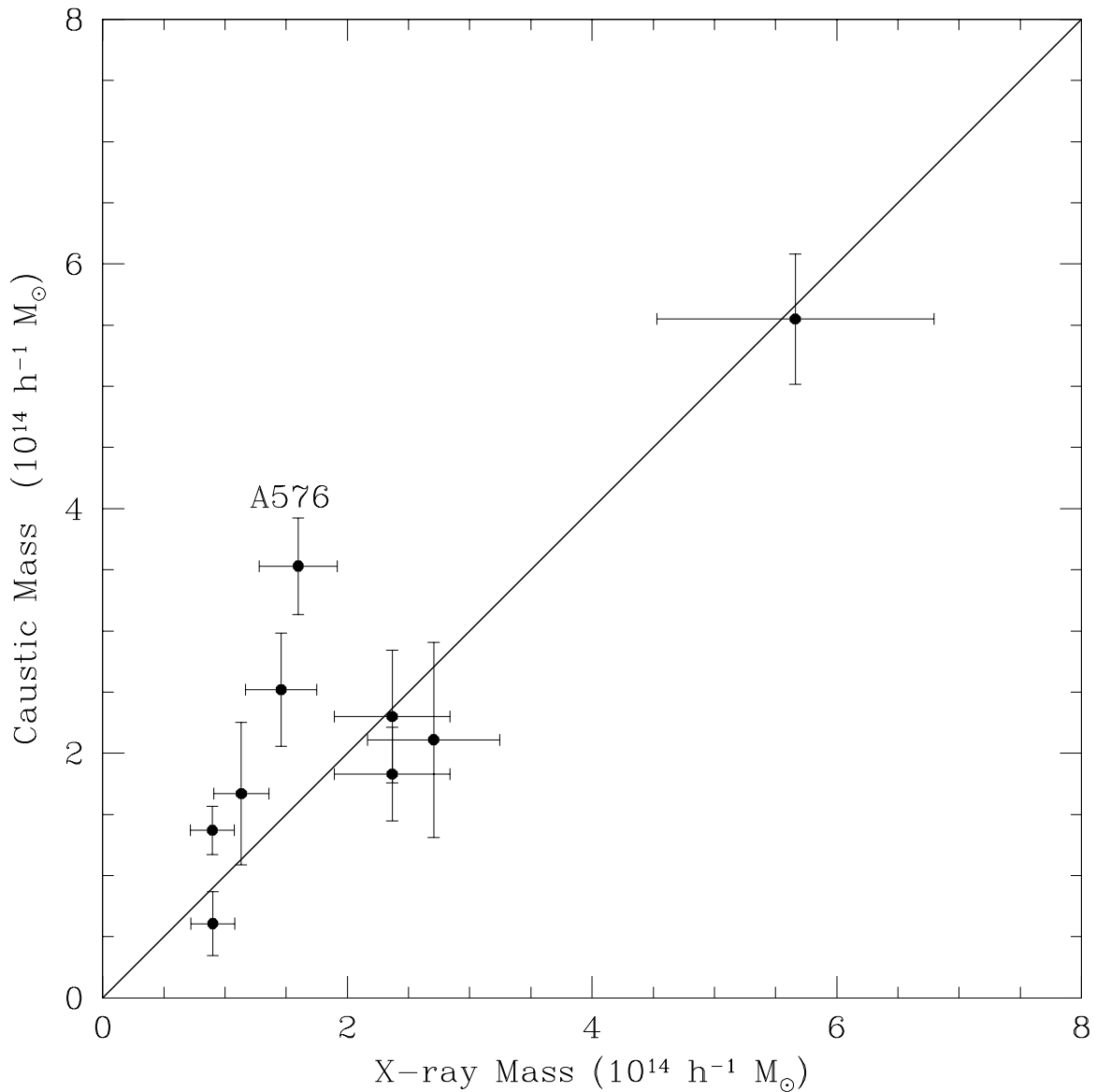


Fig. 8.— Comparison of caustic mass estimates to estimates based on the mass-temperature relation. The solid line has a slope of unity and intercepts the origin.

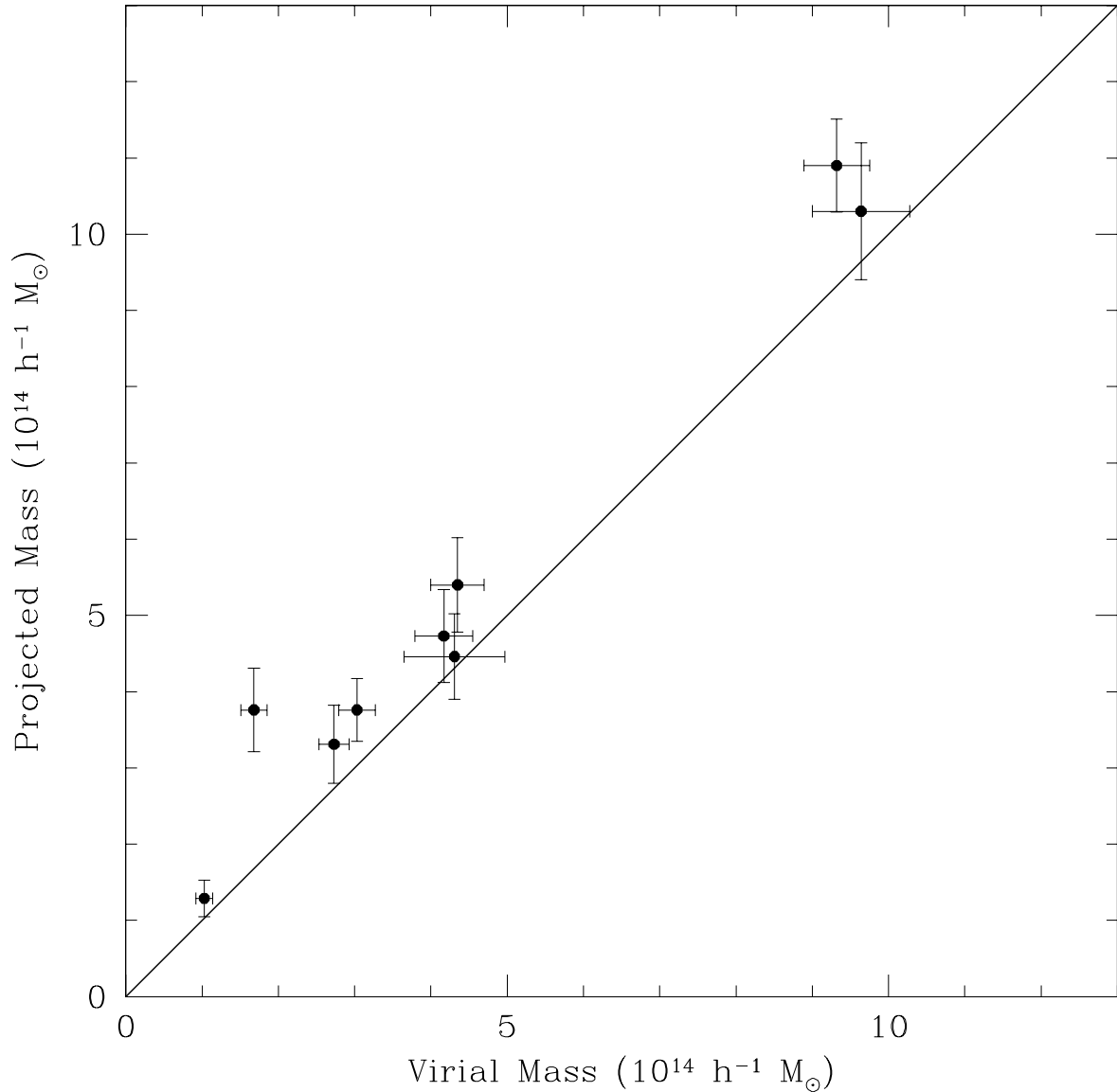


Fig. 9.— Comparison of projected mass estimates to virial mass estimates. The solid line has a slope of unity and intercepts the origin.

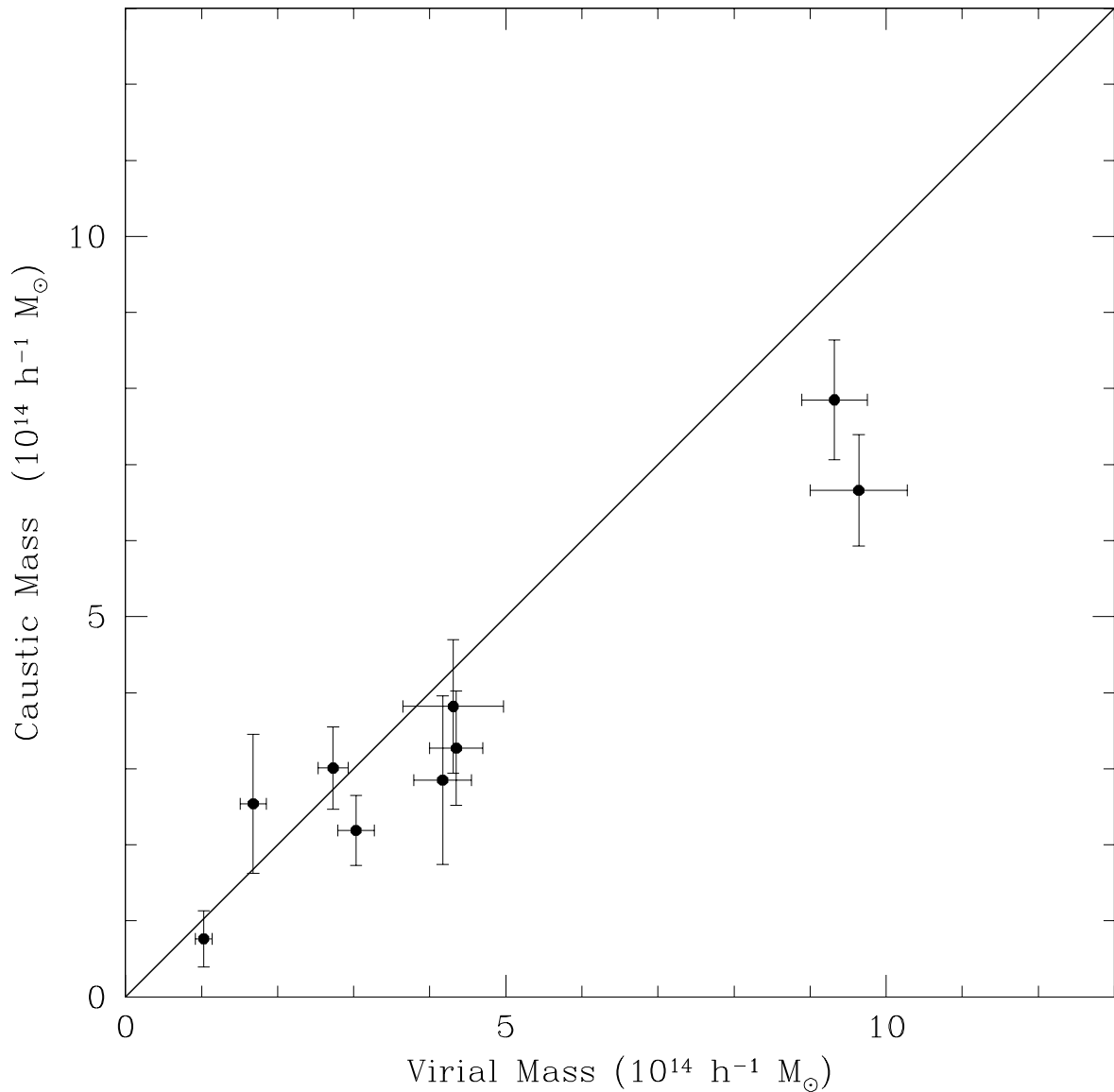


Fig. 10.— Comparison of caustic mass estimates to estimates based on the virial theorem. The solid line has a slope of unity and intercepts the origin.

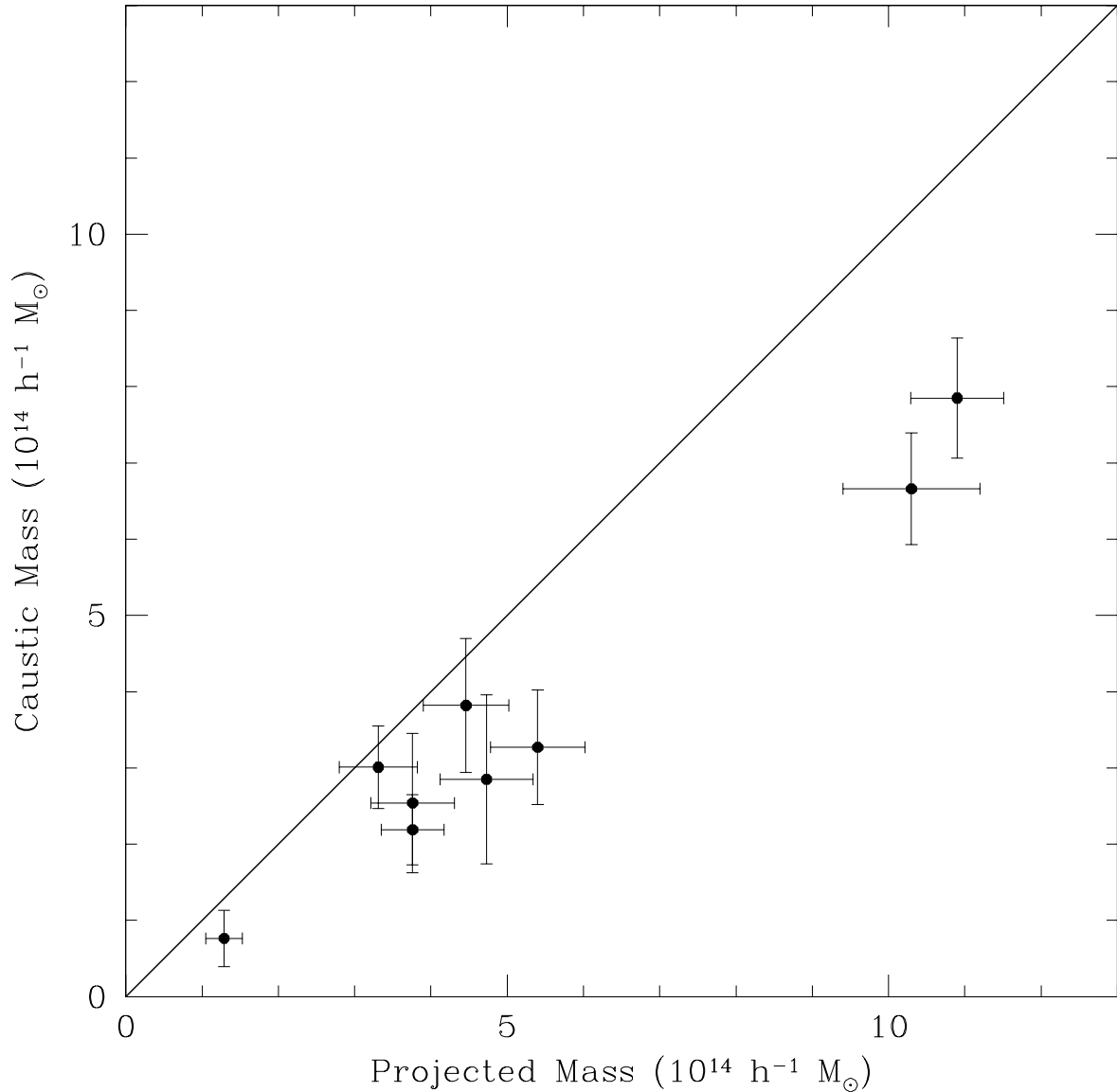


Fig. 11.— Comparison of caustic mass estimates to estimates based on the projected mass estimator. The solid line has a slope of unity and intercepts the origin.

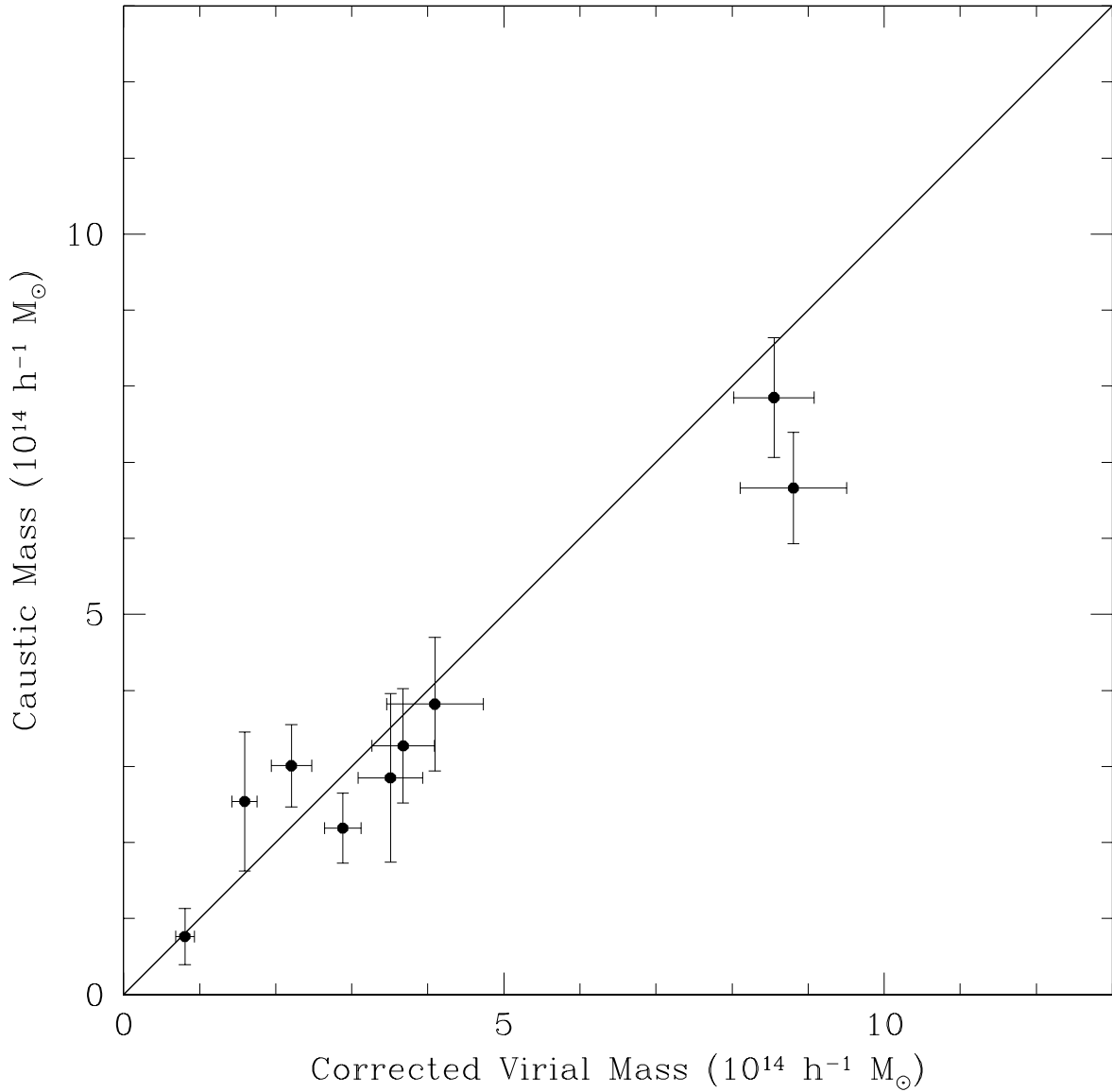


Fig. 12.— Comparison of caustic mass estimates to estimates based on the virial mass estimator with a correction for the surface pressure term. The solid line has a slope of unity and intercepts the origin.

Table 1: CAIRNS BASIC PROPERTIES

Cluster	X-ray Coordinates		cz_{\odot}	$\sigma_p(3\sigma)$	$\sigma_p(caustics)$	$L_X/10^{43}$	T_X	Richness
	RA (J2000)	DEC (J2000)	km s^{-1}	km s^{-1}	km s^{-1}	erg s^{-1}	keV	
A119	00 56 12.9	-01 14 06	13268	698_{-31}^{+36}	619_{-36}^{+44}	8.1	5.1	1
A168	01 15 08.8	+00 21 14	13395	579_{-30}^{+36}	531_{-32}^{+39}	2.7	2.6	2
A496	04 33 35.2	-13 14 45	9900	721_{-30}^{+35}	598_{-30}^{+36}	8.9	4.7	1
A539	05 16 32.1	+06 26 31	8717	734_{-44}^{+53}	717_{-48}^{+60}	2.7	3.0	1
A576	07 21 31.6	+55 45 50	11510	1009_{-36}^{+41}	881_{-38}^{+44}	3.5	3.7	1
A1367	11 44 36.2	+19 46 19	6495	782_{-46}^{+56}	745_{-43}^{+52}	4.1	3.5	2
A1656	12 59 31.9	+27 54 10	6973	1042_{-30}^{+33}	957_{-28}^{+30}	18.0	8.0	2
A2199	16 28 39.5	+39 33 00	9101	796_{-33}^{+38}	722_{-32}^{+37}	9.1	4.7	2
A194	01 25 50.4	-01 21 54	5341	495_{-33}^{+41}	402_{-29}^{+38}	0.4	2.6	0

Table 2: CAIRNS REDSHIFT CATALOGS

Cluster	R_{max}	cz_{\odot}	σ_p	N_{cz}	N_{CAIRNS}	N_{mem}
	Degrees	km s^{-1}	km s^{-1}			
A119	5	13268 ± 47	619_{-36}^{+44}	3381 ^a	669 ^a	121
A168	5	13395 ± 46	531_{-32}^{+39}	3557 ^a	525 ^a	117
A496	5	9900 ± 46	598_{-30}^{+36}	1043	515	169
A539	10	8717 ± 68	717_{-48}^{+60}	796	360	91
A576	5	11510 ± 54	881_{-38}^{+44}	1209	529	233
A1367	10	6495 ± 71	745_{-43}^{+52}	1864	502	128
A1656	10	6973 ± 45	957_{-28}^{+30}	4159	1239	548
A2199	6.5	9101 ± 50	722_{-32}^{+37}	1539	820	218
A194	10	5341 ± 51	402_{-29}^{+38}	6916 ^a	—	75

^aOverlapping samples. See text for details.

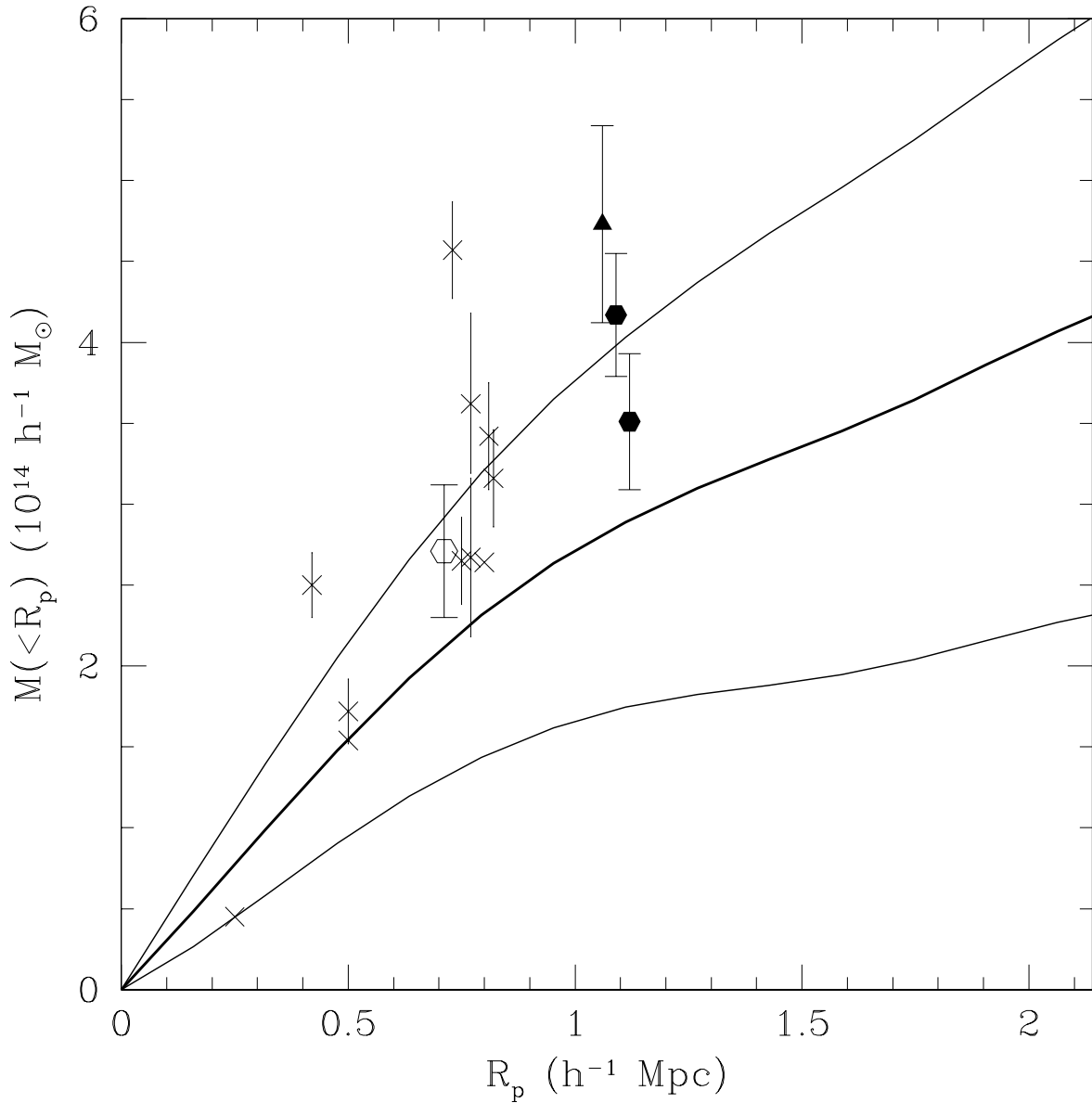


Fig. 13.— Mass profile of A119. Thick and thin solid lines show the caustic mass profile and the $1-\sigma$ uncertainties. Crosses show X-ray estimates, the open hexagon is the estimate from the $M_{500} - T_X$ relation, the triangle is the projected mass, and the filled hexagons show the virial mass with and without correction for the surface pressure term.

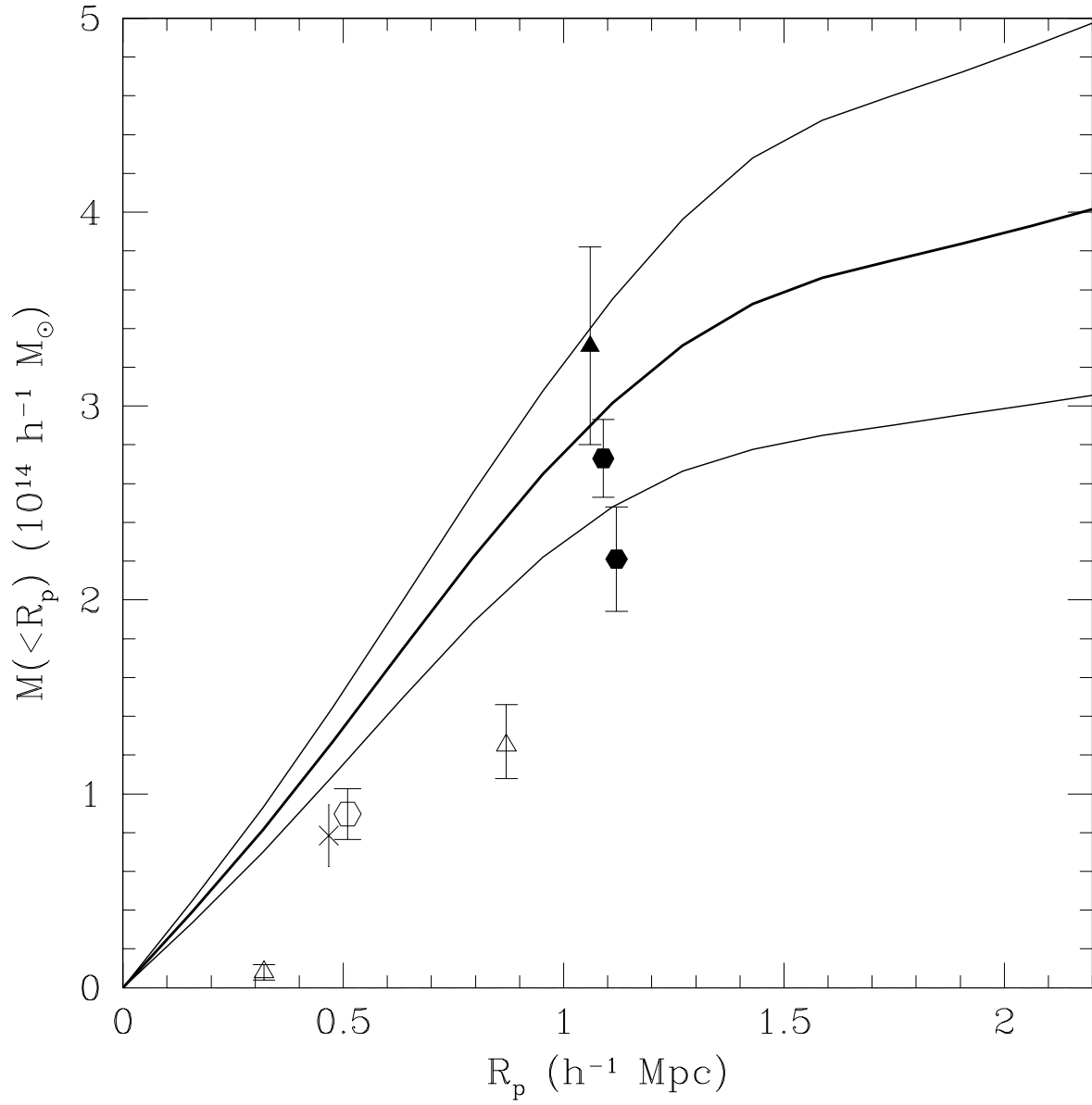


Fig. 14.— Same as Figure 13 for A168. The open triangles indicate the mass estimates of Girardi et al. (1998). See text for details.

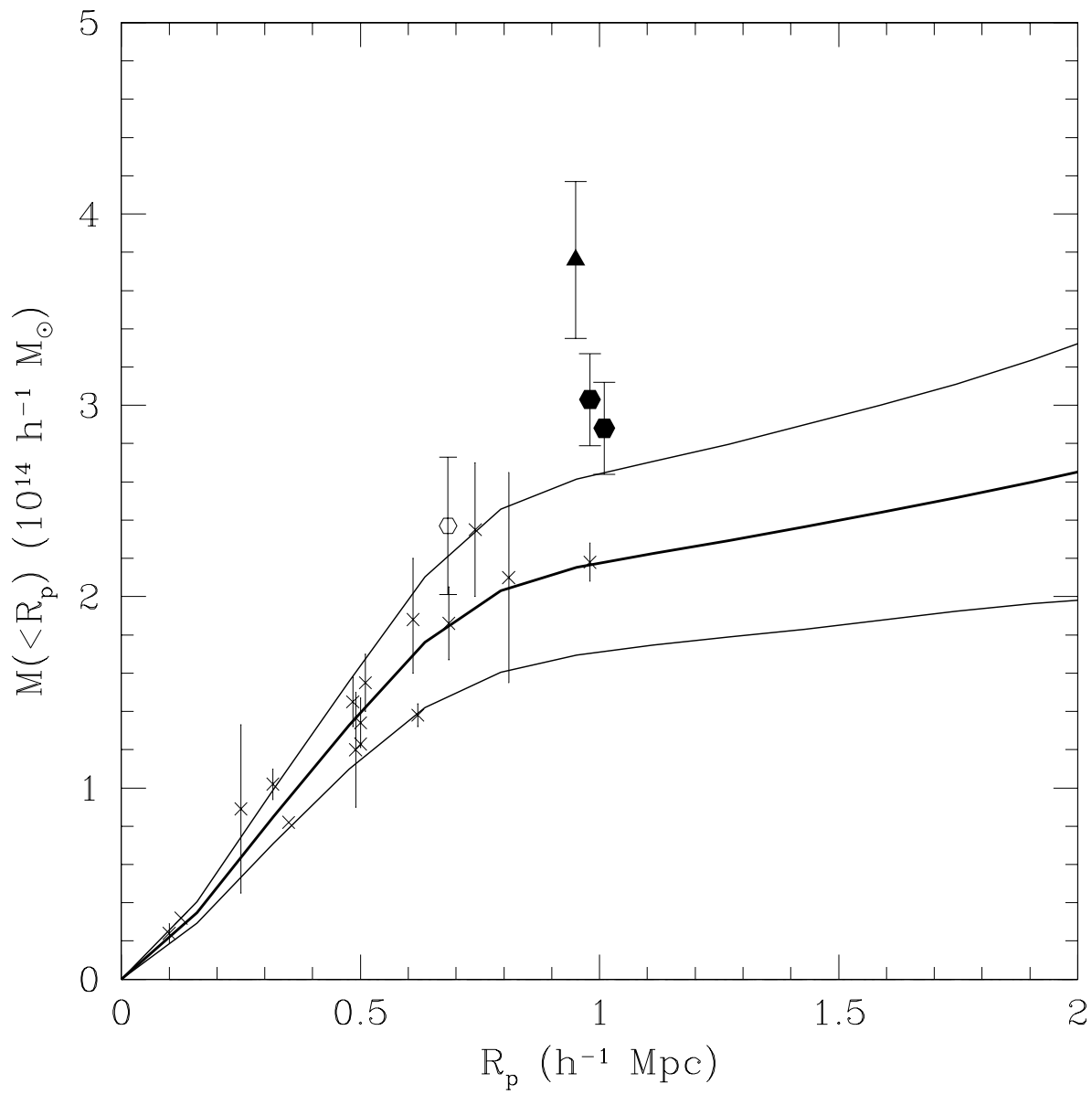


Fig. 15.— Same as Figure 13 for A496.

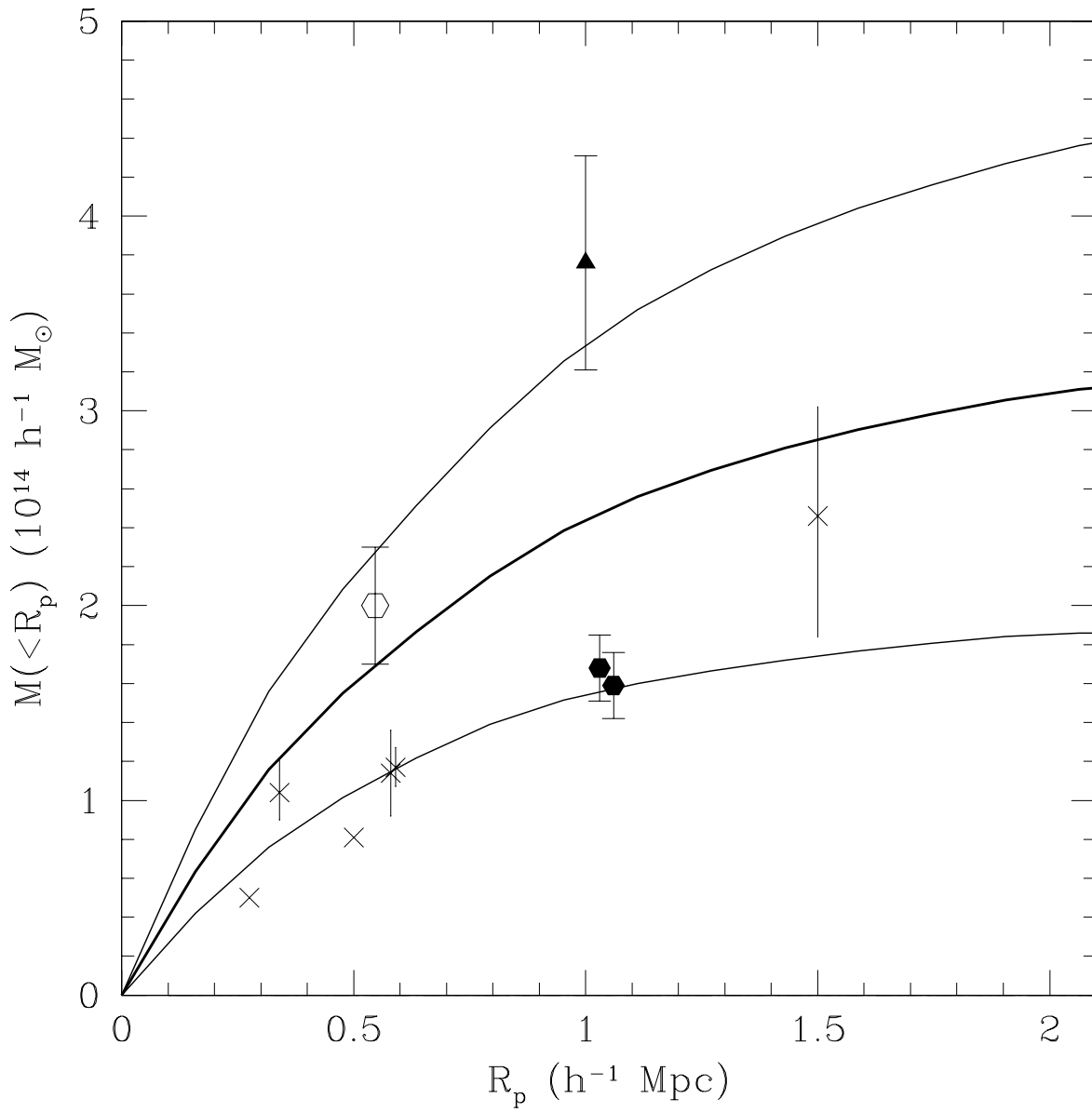


Fig. 16.— Same as Figure 13 for A539.

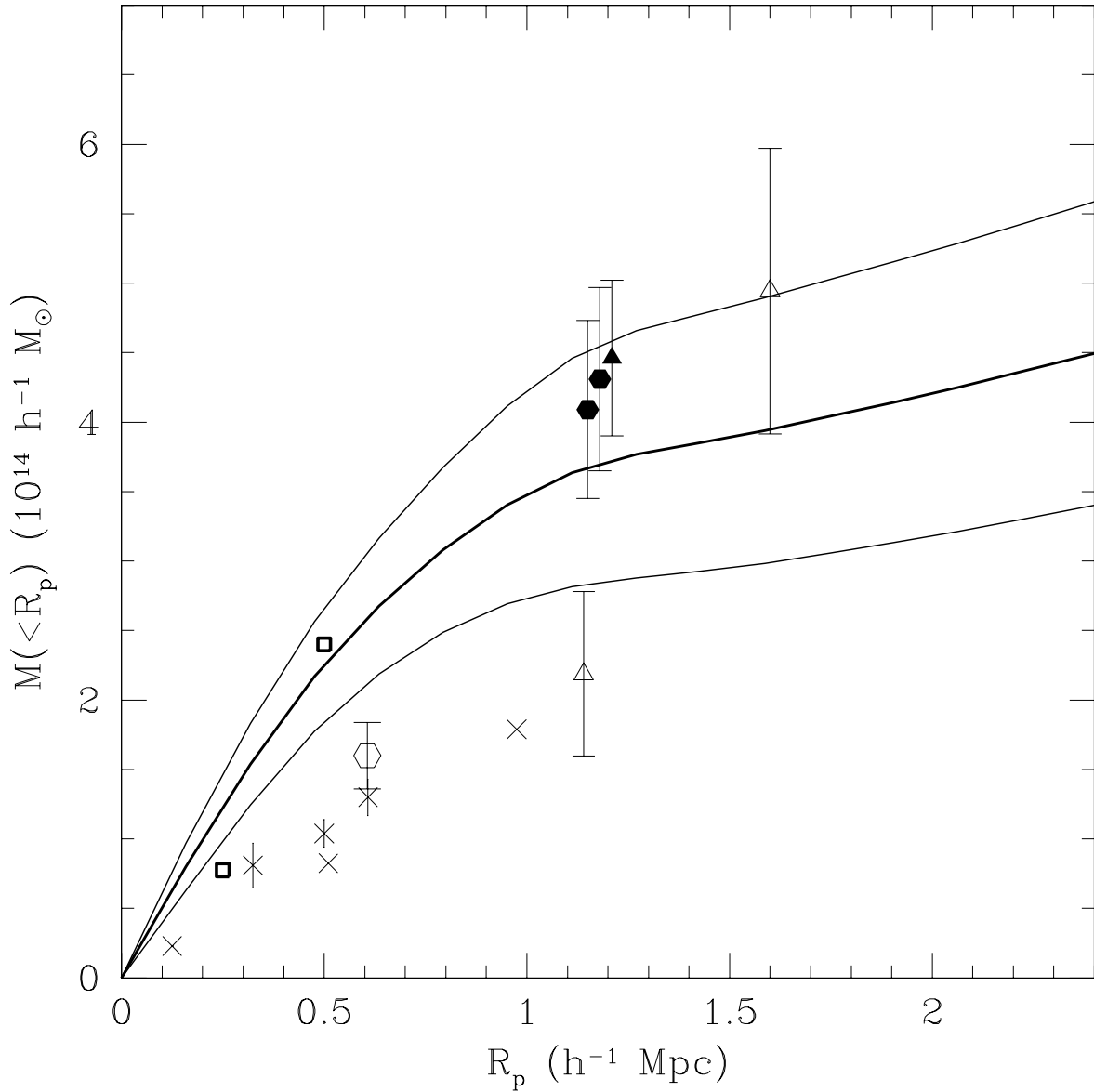


Fig. 17.— Same as Figure 13 for A1367. The open squares show the sum of the two mass components studied in Donnelly et al. (1998). The open triangles show the mass estimates of Girardi et al. (1998). See text for details.

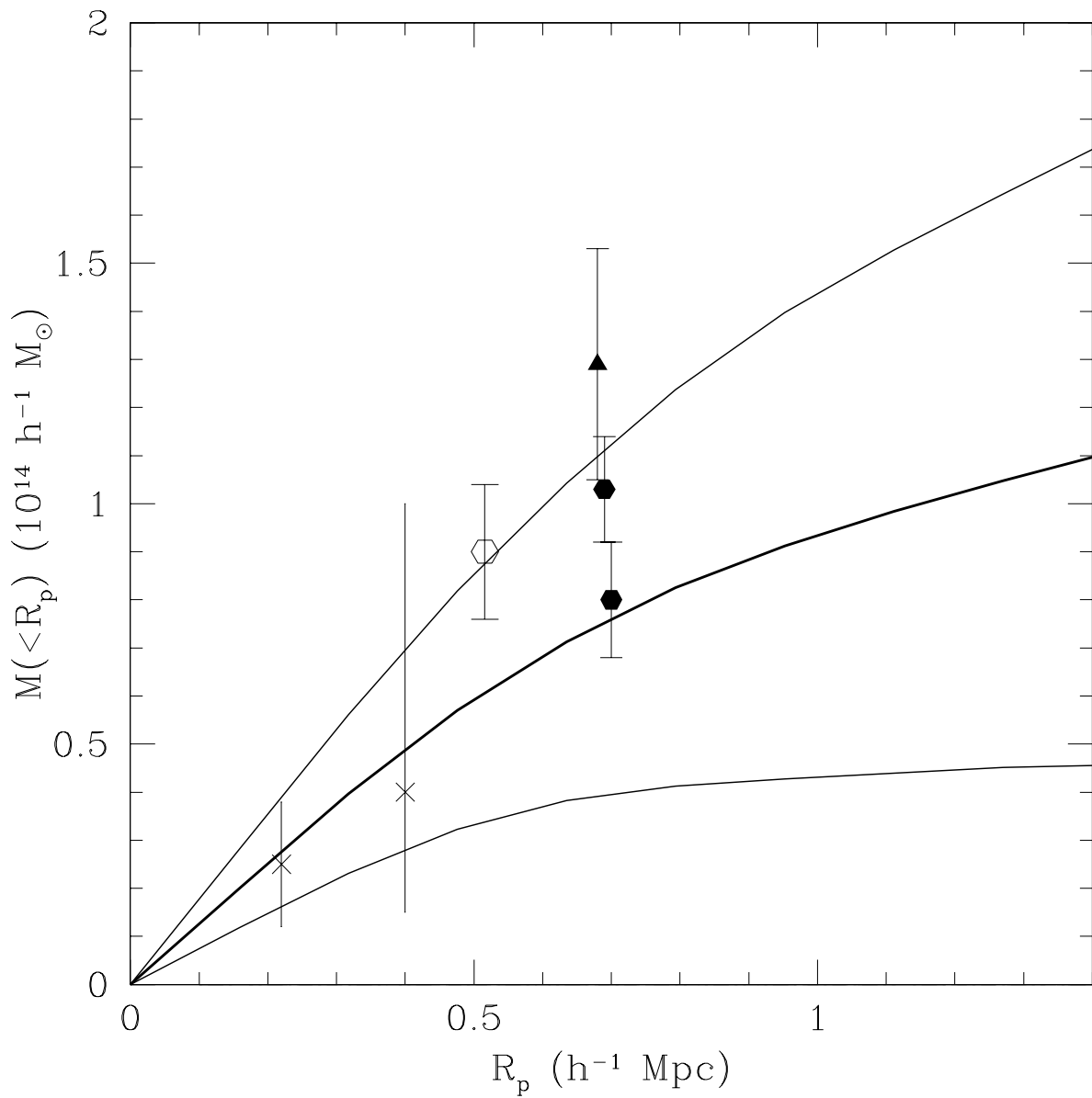


Fig. 18.— Same as Figure 13 for A194.

Table 3. Spectroscopic Data for A119 and A168^a

RA (J2000)	DEC (J2000)	cz (km s $^{-1}$)	σ_{cz} (km s $^{-1}$)	Reference	Cluster
00:36:29.23	-00:43:43.0	10214	051	3	A119
00:36:34.18	-01:04:46.6	33134	036	3	A119
00:36:45.36	-00:40:00.5	32774	040	3	A119
00:36:48.36	-00:37:27.1	48774	046	3	A119
00:36:54.22	-00:06:39.2	51401	019	3	A119

^aThe complete version of this table is in the electronic edition of the Journal. The printed edition contains only a sample.

References. — (1) FAST spectra; (2) NED; (3) SDSS.

Table 4. Spectroscopic Data for A194^a

RA (J2000)	DEC (J2000)	cz (km s $^{-1}$)	σ_{cz} (km s $^{-1}$)	Reference	Cluster
00:45:40.45	-00:52:16.6	32739	050	2	A119
00:45:44.11	-00:50:37.6	31930	037	2	A119
00:45:44.78	-01:05:20.8	20175	012	2	A119
00:45:46.72	-01:06:40.3	35461	042	2	A119
00:45:47.95	-00:51:10.1	32949	040	2	A119

^aThe complete version of this table is in the electronic edition of the Journal. The printed edition contains only a sample.

References. — (1) FAST spectra; (2) NED.

Table 5. Spectroscopic Data for A496^a

RA (J2000)	DEC (J2000)	cz (km s $^{-1}$)	σ_{cz} (km s $^{-1}$)	Reference
04:14:01.49	-13:23:23.8	09337	000	02
04:14:08.57	-13:08:34.9	09622	032	01
04:14:32.78	-13:11:02.4	08656	040	01
04:14:36.00	-13:10:29.7	09098	038	02
04:14:36.08	-13:19:01.6	08566	016	01

^aThe complete version of this table is in the electronic edition of the Journal. The printed edition contains only a sample.

References. — (1) FAST spectra; (2) NED.

Table 6. Spectroscopic Data for A539^a

RA (J2000)	DEC (J2000)	cz (km s $^{-1}$)	σ_{cz} (km s $^{-1}$)	Reference
04:38:58.98	05:37:11.3	08310	005	2
04:39:00.60	07:16:05.0	73509	150	2
04:39:02.26	05:20:43.7	62357	300	2
04:39:45.10	03:01:57.0	04518	030	2
04:39:51.50	07:03:19.0	04693	007	2

^aThe complete version of this table is in the electronic edition of the Journal. The printed edition contains only a sample.

References. — (1) FAST spectra; (2) NED.

Table 7. Spectroscopic Data for A1367^a

RA (J2000)	DEC (J2000)	cz (km s $^{-1}$)	σ_{cz} (km s $^{-1}$)	Reference
11:03:25.39	18:08:12.2	00979	004	2
11:03:38.70	19:19:43.1	09174	050	2
11:04:17.20	18:03:54.0	56961	000	2
11:04:32.20	17:07:40.1	13028	061	2
11:04:36.20	21:24:18.0	56241	087	2

^aThe complete version of this table is in the electronic edition of the Journal. The printed edition contains only a sample.

References. — (1) FAST spectra; (2) NED.

Table 8. Spectroscopic Data for Coma^a

RA (J2000)	DEC (J2000)	cz (km s $^{-1}$)	σ_{cz} (km s $^{-1}$)	Reference
12:15:03.51	29:06:02.3	31301	38	2
12:15:06.90	29:01:10.0	7445	72	2
12:15:15.77	28:50:31.0	57063	67	2
12:15:16.12	29:15:07.1	40917	66	2
12:15:23.17	26:53:05.6	7518	24	1

^aThe complete version of this table is in the electronic edition of the Journal. The printed edition contains only a sample.

Table 9: CAIRNS HIERARCHICAL CENTERS

Cluster	Hierarchical Center		cz_{cen} km s $^{-1}$	ΔR h^{-1} kpc
	RA (J2000)	DEC (J2000)		
A119	00 56 10.1	-01 15 20	13278	56
A168	01 15 00.7	+00 15 31	13493	239
A496	04 33 38.6	-13 15 47	9831	24
A539	05 16 37.0	+06 26 57	8648	33
A576	07 21 32.0	+55 45 21	11487	16
A1367	11 44 49.1	+19 46 03	6509	61
A1656	13 00 00.7	+27 56 51	7093	153
A2199	16 28 47.0	+39 30 22	9156	86
A194	01 25 48.0	-01 21 34	5317	11

Table 10: CAIRNS VIRIAL AND TURNAROUND RADII

Cluster	r_{200} h^{-1} Mpc	r_t h^{-1} Mpc	M_{200} $10^{13} M_\odot$	M_t $10^{13} M_\odot$	M_t/M_{200}
A119	1.07	5.4	28.5	63	2.2
A168	1.09	5.5	30.1	66	2.2
A496	0.98	4.2	21.9	30	1.4
A539	1.03	4.3	25.4	32	1.2
A576	1.42	6.0	66.6	88	1.3
A1367	1.18	5.2	38.2	56	1.5
A1656	1.50	7.4	78.5	165	2.1
A2199	1.12	5.3	32.7	58	1.8
A194	0.69	3.3	7.6	15	2.0

Table 11: CAIRNS MASS PROFILE FIT PARAMETERS

Cluster	Form	R_{max} $h^{-1}\text{Mpc}$	a $h^{-1}\text{Mpc}$	1σ $h^{-1}\text{Mpc}$	$M(a)$ $10^{13}M_\odot$	1σ $10^{13}M_\odot$	χ^2	ν
A119	NFW	5.4	0.17	0.10-0.27	4.9	3.7-6.4	0.04	32
	Hernquist	5.4	0.58	0.44-0.62	17.5	15.0-21.5	0.51	32
	SIS	5.4	0.50	–	8.4	7.8-9.2	12.5	33
A168	NFW	5.5	0.21	0.17-0.25	5.2	4.6-5.8	2.39	32
	Hernquist	5.5	0.65	0.57-0.71	18.0	16.4-19.2	1.97	32
	SIS	5.5	0.50	–	8.2	8.0-8.6	67.8	33
A496	NFW	4.0	0.07	0.05-0.10	2.1	1.8-2.5	2.67	24
	Hernquist	4.0	0.31	0.26-0.38	8.9	8.2-9.9	0.73	24
	SIS	4.0	0.50	–	6.2	5.9-6.6	62.6	25
A539	NFW	2.5	0.07	0.04-0.13	2.4	1.8-3.5	0.13	15
	Hernquist	2.5	0.25	0.17-0.44	9.5	7.9-12.6	0.16	15
	SIS	2.5	0.50	–	9.3	7.4-10.8	12.4	16
A576	NFW	4.3	0.13	0.12-0.14	7.4	6.9-7.9	7.60	26
	Hernquist	4.3	0.43	0.40-0.46	26.9	25.7-28.0	1.64	26
	SIS	4.3	0.50	–	15.7	15.4-16.1	189	27
A1367	NFW	5.2	0.07	0.05-0.09	3.3	2.9-3.7	1.37	31
	Hernquist	5.2	0.29	0.25-0.34	14.5	13.5-15.5	0.88	31
	SIS	5.2	0.50	–	8.1	7.7-8.4	99.3	32
A1656	NFW	7.4	0.15	0.14-0.17	10.3	9.7-11.0	2.46	45
	Hernquist	7.4	0.53	0.48-0.55	38.6	36.7-40.2	22.4	45
	SIS	7.4	0.50	–	18.6	18.3-19.1	292	46
A2199	NFW	4.1	0.15	0.11-0.19	4.7	4.0-5.5	0.50	25
	Hernquist	4.1	0.47	0.39-0.57	16.7	15.0-18.5	1.21	25
	SIS	4.1	0.50	–	9.8	9.3-10.2	30.8	26
A194	NFW	3.3	0.11	0.06-0.19	1.3	0.9-1.8	0.01	19
	Hernquist	3.3	0.35	0.24-0.52	4.5	3.4-5.8	0.26	19
	SIS	3.3	0.50	–	3.7	3.2-4.1	6.01	20

Table 12: CAIRNS VIRIAL AND PROJECTED MASSES

Cluster	r_{200} $h^{-1}\text{Mpc}$	M_{200} $10^{13}M_\odot$	M_{proj} $10^{13}M_\odot$	M_{vir} $10^{13}M_\odot$	M_{cv} $10^{13}M_\odot$
A119	1.07	28.5	47.3 ± 6.1	41.7 ± 3.8	35.1 ± 4.2
A168	1.09	30.1	33.1 ± 5.1	27.3 ± 2.0	22.1 ± 2.7
A496	0.98	21.9	37.6 ± 4.1	30.3 ± 2.4	28.8 ± 2.4
A539	1.03	25.4	37.6 ± 5.5	16.8 ± 1.7	15.9 ± 1.7
A576	1.42	66.6	103.0 ± 9.0	96.4 ± 6.4	88.0 ± 7.0
A1367	1.18	38.2	44.6 ± 5.6	43.1 ± 6.6	40.9 ± 6.4
A1656	1.50	78.5	109.0 ± 6.1	93.2 ± 4.3	85.5 ± 5.3
A2199	1.12	32.7	54.0 ± 6.2	43.5 ± 3.5	36.8 ± 4.1
A194	0.69	7.6	12.9 ± 2.4	10.3 ± 1.1	8.0 ± 1.2